Escuela de Caminos
Escuela Técnica Superior de Ingenieros de Caminos, Canales y Puertos
UPC BARCELONATECH

TRABAJO FINAL DE MASTER

Desarrollo de nuevos métodos para el análisis fluido-estructura mediante PFEM

Trabajo realizado por:
Joaquín González Usúa

Dirigido por:
Eugenio Oñate Ibañez de Navarra
Ignasi de Pouplana Sardà

Máster en:
Ingeniería de Caminos, Canales y Puertos

Barcelona, a 14 de junio de 2019

Departamento de Ingenería Civil y Ambiental

Abstract

This thesis presents a new PFEM-DEM coupling strategy to solve fluid-structure interaction problems. The free-surface fluid is solved using the Particle Finite Element Method (PFEM) in a fully Lagrangian two step velocity-pressure scheme. Solid particles are considered in the problem as discrete elements (DEM) embedded in the fluid.

Given that DEM is solved in a explicit way and PFEM is solved implicitly, the coupling between them can be complex. Usually, the time step of the fluid is two or three order higher than the time step used to compute the solid particles and so, to obtain accurate results,a sub-stepping algorithm is performed to solve DEM at each fluid time step.

The scheme proposed has been validated using three different tests including numerical simulations, analytical solutions and experimental results showing a good agreement with the coupling scheme proposed.

For the cases solved in this work, an one way coupling algorithm can be used because the effect of the particles is considered negligible for the fluid solutions. However, there are other examples where the particles must modify the permeability of the medium and thus the forces of the particles over the fluid must be accounted. This is called two way coupling and the complexity of the PFEM-DEM coupling increases significantly.

Apart from the presented strategy, a PFEM-DEM coupling using a monolithic ALE fluid is currently being developed. This alternative strategy should let us impose easily slip conditions providing more accurate results when working with coarse meshes.

Contents

1 Introduction

Problems that couple fluid with deformable structures, rigid bodies or solid particles have received notable attention in the last decades mainly because of their importance in modelling natural disasters such as floods, landslides or fractures in dams. These models can be conveniently designed to study the behaviour of a structure when a disaster occurs and the damages produced on it, the soil erosion or the settlement of particles.

In those simulations, solid particles are considered as rigid and immiscible and have a size very small in comparison with the characteristic length of the fluid element. The coupling between solid particles and the fluid surrounding them can be used, for instance, to analyse the impacts of a solid in a structure such as a dam, a dock or a pipeline. Another useful application is to evaluate the amount of solid that can be eroded when a landslide occurs and the possible areas that can affect in order to make predictions to select the safest areas for evacuation.

The aim of this work is to provide simplified models to test PFEM-DEM coupling that can be applied for other examples. In some cases shown below, experimental results have been used to validate them. The objective is to develop a scheme which can be used to analyse sedimentations of solid particles in a fluid flow and the behaviour of those particles embedded in a fluid. One possible application found is to use the particles as tracers of the fluid in order to obtain the stream lines of it.

With the purpose of suiting the objectives of the document, a Lagrangian approach has been used in one way coupling. The modification produced in the mass of the fluid during the simulations has not been taken into account.

In the case of the ALE formulation, an example based in an experiment will be shown. In this scheme, a monolithic way to solve the fluid will be used. Special attention is paid in the interaction between the elements located in the free surface and the rigid walls to avoid problems relating to isolated elements. The criteria to select the valid elements to be used and the interface between the Lagrangian and Eulerian approach in the fluid will be critical to obtain accurate results for the method.

This thesis is organised as follows: the first section will be the state of the art for fluid-interaction problems, PFEM, DEM and PFEM-DEM coupling as a brief review of the developments made until now. In the next section the governing equations for fluids focusing on the Lagrangian approach will be developed together with the equations for DEM. In this section the method for stabilization, the neighboring strategy and the remeshing method will be discussed as well. Section three provides a description of the examples and the results obtained and finally, the conclusions and future lines will be discussed in the section 4 in which ALE scheme is being developing to make easier the imposition of slip boundaries, so it is interesting to couple with DEM particles.

This work has been done inside Kratos framework which is an open source platform written in C++ for the numerical computation and Python for the interface. The usage of Kratos lets simulate using a parallel architecture and reducing the computation time to obtain results. The structure of Kratos is defined by a core where the basic and general tools are located and application in which specific methods and utilities are located. For the present report, the scheme of Kratos could be defined as in the Figure 1.

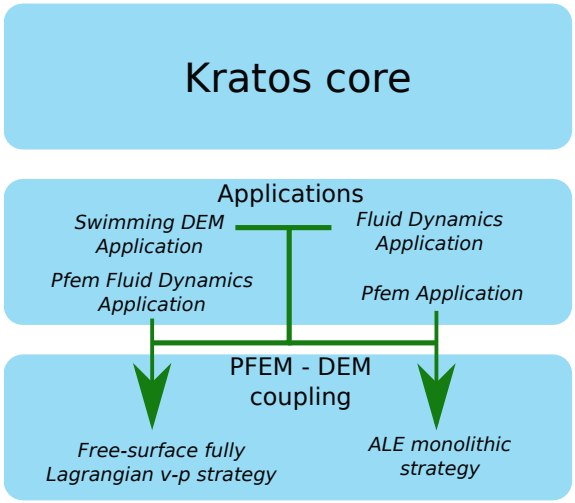

Figure 1: Kratos scheme used for PFEM-DEM coupling

2 State of art

The interest in developing numerical methods to solve the fluid-structure interaction started to evaluate the safety of the nuclear reactors. To do that, finite elements were used to model the continuum fluid [1]. First works used a Lagrangian approach to simulate the fluid even though the mixed methods -which utilize Eulerian-Lagrangian- were developed before to solve hydrodynamic problems.

The first paper in which a mixed solution was proposed to solve a two dimensional Eulerian hydrodynamic problem using a non fixed fluid boundary. They took advantage of the accuracy and the low computational cost -due to the use of a reduce number of nodes- of the Lagrangian approach. Its weakness due to the turbulent zones that led to distorsions in the mesh disappeared. Finally, the solution consisted in solving subregions near to the structure using the Eulerian approach and the Lagrangian one in the rest [2].

Furthermore, Hirt *et al.* [3] solved the Navier-Stokes equations applied to flows for any velocity. In that work, a finite differences mesh capable to move at the same velocity as the fluid, be fixed or move to any other velocity was used. This method is the so-called *"Arbitrary-Lagrangian-Eulerian"* or ALE. This method, initially proposed to solve fluid problems, was used for the resolution of bidimensional fluid-structure interaction subject to a dynamic and transitory load. In this case, the coupling was developed letting the fluid mesh move independently on the solid meshes. However, an alignment between the fluid and solid nodes was imposed to make easier the information transfer [4]. In another research, ALE system was used to couple a fluid with particles to simulate the settlement of cylinders in a channel. To do that, Navier-Stokes equations were used to solve the liquid phase and the Newtonian movement equations in the case of the solid bodies [5]. This method has been considered in problems where the domain formed by the fluid suffers huge deformations like in the case of an artificial heart [6].

It is important to highlight the combination of a purely Lagrangian approach and ALE such as it was carried out in [7]. In this research, it was utilized a particle formulation to model free surfaces, the contact of a solid and a fluid or any interface and the ALE formulation for the rest of the domain, which let internal nodes avoid the deformation of the mesh produced by the vortices or important velocity gradients.

In the present document, the solution of the fluid phase will be computed using the so-called *"particle finite element method"*. This technique was developed by Oñate *et al.* [8] to evaluate every fluid particle from a Lagrangian point of view leading to solve fluid-rigid solid interaction problems.

The initial ideas come from astrophysics in a trial to improve the accuracy in the results using fewer nodes in the mesh. To get the point, it was implemented a method which uses the Lagrangian approach for the fluid in a way that the subregions of the fluid can move following the Newtonian movement equations [9]. Due to problems in the results

that were obtained from the finite elements, Nayroles *et al.* [10] proposed methodologies to provide better approximations without the necessity to use elements, only nodes, for this reason, those received the name *"Meshless Method"*. One of them, the so-called *"Finite Point Method"* in which the interpolation is obtained by using least squares was used to solved fluid mechanics problems [11].

The *"Particle Finite Element Method"* was proposed using a particle method together with the finite element method. Regarding this formulation, it has been modeled the bed erosion based on the friction generated between the bed surface and the tangential stress of the fluid, a rock-fill dam, the erosion in the land surrounding a bridge pile [12] or the impact of the waves in a breakwater [13]. In other work, it was modeled the effect of an earthquake produced in the Lituya Bay reservoir obtaining results with less than a 5% of error for the maximum water height after a landslide [14] showing that this method is good at solving fluid-structure interaction problems as well.

In relation to the solid particles, the *"Discrete Element Method"* or DEM will be used. It was developed in the seventies decade of the twentieth century with the objective of modelling granular mediums which let calculate and measure the internal stresses and displacements in them. This method leads to regard the interaction between particles as a transitory problem when the internal forces are in equilibrium [15]. In geomechanics, this method has been combined with FEM to simulate the rock failure. In this case, FEM was utilized to model the continuum while DEM simulated the discontinuities produced by the loss of cohesion between particles [16].

For the case of resolution of fluid-particle interaction by using discrete elements, the first simulations were carried out by Johnson *et al.* [17] who used those elements to simulate the particles and a formulation of finite elements stabilized for space and time to model the fluid. In that paper, the solid particles had to fall in a pipe with fluid. In other work, it was proposed to solve system with fluid-particles strong coupling involving a huge number of solid particles embedded in a fluid [18]. In this kind of problems, it has been developed strategies based on weak coupling to calculate forces produced by the interaction between particles. Although this type of formulation could be more appropriate, the computational cost is higher than in the case of strong coupling [19]. Other works have tried to solve these problems combining PFEM and DEM, for instance in [20] where the transport of particles around a drill was modelled.

3 Methodology

In this section, the methodology used in this document will be defined. First, the main fluid mechanics equations applied in Lagrangian approach will be shown, after that, the basis of the two step velocity-pressure strategy and DEM method will be explained together with the discretized equations applied.

3.1 PFEM fluid formulation

3.1.1 Governing equations

3.1.1.1 Strong form of the fluid equations

In the Lagrangian approach, the mesh would be embedded in the fluid and it moves at the same velocity as the fluid, for this reason, this scheme is defined by its material coordinates. The governing equations for fluid dynamics are the mass conservation law and momentum conservation law which can be defined as follows:

$$\frac{\partial \rho}{\partial t} = -\rho \nabla \cdot v \tag{1}$$

and

$$\rho \frac{\partial v_i}{\partial t} = b_i - \frac{\partial p}{\partial x_i} \tag{2}$$

where the equation (1) is the mass conservation law and the expression (2) is the momentum conservation. It is important to highlight that the stress term p is the *"Cauchy estress tensor"* (σ_{ij}). At the moment to define this term, it will regard first a discrete system of particles and a force acting in every particle i with the form $f_i = m_i a_i$. It has to be taken into account that the tensor in the fluid is divided in a deviatoric part (s_{ij}) and the pressure (p) so the expression is as follows

$$\sigma_{ij} = s_{ij} + p\delta_{ij} \tag{3}$$

as in this document, only Newtonian fluids will be used, the relation between the deviatoric stress and the deformation rate for this type of fluid will be considered, then

$$s_{ij} = 2\mu\varepsilon'_{ij} \tag{4}$$

$$\varepsilon'_{ij} = \varepsilon_{ij} - \frac{1}{3}\varepsilon_v \delta_{ij} \tag{5}$$

where μ is the velocity that will be regarded as a constant when Newtonian fluids are used, for this reason, the relation between the stress and the deformation is lineal. δ_{ij} is

Kroneker delta, ε'_{ij} is the deviatoric part and ε_v is the volumetric one for the deformation rate, furthermore, the deformation is

$$\varepsilon_{ij} = \frac{1}{2}\left(\frac{\partial v_i}{\partial x_j} + \frac{\partial v_j}{\partial x_i}\right) \tag{6}$$

However, in the present document, it will be used a quasi-incompressible particle fluid, for this reason, the expressions (1) and (2) will include variables such as the bulk parameter κ. In addition, it has to be taken into account the interaction forces between the fluid and particle. Regarding these variables, the equation aforementioned can be expressed, in the following way [20]

$$-\frac{1}{\kappa}\frac{\partial p}{\partial t} + \frac{1}{n_f}\frac{\partial n_f}{\partial t} + \varepsilon_v = 0 \tag{7}$$

$$\rho\frac{\partial v_i}{\partial t} - \frac{\partial \sigma_{ij}}{\partial x_j} - \left(b_i - \frac{1}{n_f}f_i^{pf}\right) = 0 \tag{8}$$

where equation (7) is the mass conservation law, equation (8) is the linear momentum equation, f_i^{pf} are the fluid-particle interaction forces, κ is the bulk parameter that in quasi-incompressible fluid is fluid density and speed of sound function ($\kappa = \rho c^2$) [21]. Finally, the volume fluid fraction (n_f) in a point for every node is described as follows

$$n_{f_j} = 1 - \frac{1}{V_j}\sum_{i=1}^{n_j} V_j^i \tag{9}$$

in which V_j is the representative domain associated to the node j, V_j^i is the particle volume i belonging to the domain V_j and n_{f_j} is the number of particles inside the domain [20]. If now the expression $r_{mi} := \rho\frac{\partial v_i}{\partial t} - \frac{\partial \sigma_{ij}}{\partial x_j} - \left(b_i - \frac{1}{n_f}f_i^{pf}\right)$ is considered, the momentum equation would be defined as

$$r_{mi} - \frac{h}{2}\frac{\partial r_{mi}}{\partial x_j} = 0 \tag{10}$$

from previous works [20, 22, 23] the stability parameter necessary to match r_v and r_{mi} is obtained

$$r_v - \tau\frac{\partial r_{mi}}{\partial x_j} = 0 \quad in \quad V \tag{11}$$

being τ the stability parameter whose expression is

$$\tau = \left(\frac{8\mu}{h^2} + \frac{2\rho}{T}\right)^{-1} \tag{12}$$

and r_{mi} is equal to

$$r_{mi} := \frac{\partial \sigma_{ij}}{\partial x_j} + \left(b_i + \frac{1}{n_f}f_i^{pf}\right) \tag{13}$$

where μ is the viscosity, h is the characteristic length of the element, ρ is the fluid density and T a parameter which depends on the time and it can be substituted as $T = \Delta t$.

3.1.1.2 Weak form of the fluid equations

The mass conservation equation in its global approach is

$$\int_V \frac{1}{\kappa}\frac{\partial p}{\partial t}dV - \int_V \left(\frac{1}{n_f}\frac{\partial n_f}{\partial t} - \varepsilon_v\right)dV - \int_V \tau \frac{\partial}{\partial x_j}\left(\rho\frac{\partial v_i}{\partial t} - \frac{\partial \sigma_{ij}}{\partial x_j} - \left(b_i - \frac{1}{n_f}f_i^{pf}\right)\right)dV = 0 \quad (14)$$

to discretize the equations, the Galerkin method is used, which consists in utilizing test functions over a domain Ω. Starting with the linear momentum conservation law, the function ω will be used, therefore

$$\begin{aligned}\int_\Omega \omega\rho\frac{\partial v}{\partial t}d\Omega - \int_\Omega \omega\nabla\sigma d\Omega - \int_\Omega \omega b_i d\Omega - \int_\Omega \omega\frac{1}{n_f}f_i^{pf}d\Omega - \int_\Omega \omega\frac{h}{2}\frac{\partial r_{mi}}{\partial x_j}d\Omega = 0 \Rightarrow \\ \int_\Omega \omega\rho\frac{\partial v}{\partial t}d\Omega - \int_\Gamma \omega t d\Gamma + \int_\Omega \nabla\omega\sigma d\Omega - \int_\Omega \omega b_i d\Omega - \int_\Omega \omega\frac{1}{n_f}f_i^{pf}d\Omega - \int_\Gamma \omega\frac{h}{2}r_{mi}d\Gamma \\ + \int_\Omega \nabla w\frac{h}{2}r_{mi}d\Omega = 0\end{aligned} \quad (15)$$

it is important to take account that in the second term of the expression (14) appears a superficial force due to it is applied in the boundary of the domain and not inside. The two last terms of the aforementioned equations are null, the last one because of the usage of the Lagrangian approach and the other one because the contourn is negligible, hence, the equation (14) can be defined as

$$\int_\Omega \omega\rho\frac{\partial v}{\partial t}d\Omega - \int_\Gamma \omega t d\Gamma + \int_\Omega \nabla\omega\sigma d\Omega - \int_\Omega \omega b_i d\Omega - \int_\Omega \omega\frac{1}{n_f}f_i^{pf}d\Omega = 0 \quad (16)$$

in a analogous manner as in the momentum conservation equation, the test functions are multiplied by the conservation equation, taking in consideration that the following boundary conditions are satisfied [23]

$$\frac{2}{3}\mu\varepsilon_v = 2\mu\varepsilon_n + p - t_n \quad (17)$$

$$\frac{2}{3}\mu\frac{\partial\varepsilon_v}{\partial n} = -\frac{4\mu}{3h_n}\varepsilon_v \quad (18)$$

from the expressions (17) and (18), the final expression for both, the domain and the boundary can be obtained

$$\begin{aligned}
&\int_\Omega q\frac{1}{\kappa}\frac{\partial p}{\partial t}d\Omega - \int_\Omega q\left(\frac{1}{n_f}\frac{\partial n_f}{\partial t} - \varepsilon_v\right)d\Omega + \int_\Omega q\tau\frac{\partial}{\partial x_j}\left(\frac{\partial \sigma_{ij}}{\partial x_j} - \left(b_i - \frac{1}{n_f}f_i^{pf}\right)\right)d\Omega = 0 \Rightarrow \\
&\int_\Omega q\frac{1}{\kappa}\frac{\partial p}{\partial t}d\Omega - \int_\Omega q\left(\frac{1}{n_f}\frac{\partial n_f}{\partial t} - \varepsilon_v\right)d\Omega - \int_\Gamma q\tau\left(\rho\frac{\partial v_n}{\partial t} - \frac{2\mu}{3}\frac{\partial \varepsilon_v}{\partial n} + p - t_n + \frac{1}{n_f}f_i^{pf}\right)d\Gamma \\
&\qquad + \int_V \frac{\partial q}{\partial x_j}\tau\left(\frac{\partial}{\partial x_j}(2\mu\varepsilon_{ij}) + \frac{\partial p}{\partial x_j} + b_i + \frac{1}{n_f}f_i^{pf}\right)d\Omega = 0 \Rightarrow \\
&\int_\Omega q\frac{1}{\kappa}\frac{\partial p}{\partial t}d\Omega - \int_\Omega q\left(\frac{1}{n_f}\frac{\partial n_f}{\partial t} - \varepsilon_v\right)d\Omega - \int_\Gamma q\tau\left(\rho\frac{\partial v_n}{\partial t} - \frac{2}{h_n}\varepsilon_n + p - t_n + \frac{1}{n_f}f_i^{pf}\right)d\Gamma \\
&\qquad + \int_\Omega \frac{\partial q}{\partial x_i}\tau\left(\rho\frac{\partial v_i}{\partial t} - \frac{\partial}{\partial x_j}(2\mu\varepsilon_{ij}) + \frac{\partial p}{\partial x_j} - b_i + \frac{1}{n_f}f_i^{pf}\right)d\Omega = 0
\end{aligned} \tag{19}$$

the equation (19) defines the mass conservation law before its discretization in *FEM*. To discretize the governing equations, it is necessary to consider a stabilization method, in the present work, it will utilizaed the *"Finite Calculus Method"* or FIC.

3.1.2 FIC stabilization procedure

This method was developed by Oñate in [24] and it has been used in a wide variety of problems such as fluid-porous solid interaction [25] or problems with incompressible fluids without huge mass losses [23]. This method lets stabilize the mass balance and momentum using higher orders of the Taylor series in the terms of the aforementioned balance equations. Therefore, the derivation of the mass balance equation (17) will be derivated defining first its global form and then the Taylor series will be used for each of its terms individually, so

$$-\int_V \frac{1}{\kappa}\frac{\partial p}{\partial t}dV + \int_V \left(\frac{1}{n_f}\frac{\partial n_f}{\partial t} + \varepsilon_v\right)dV = 0 \tag{20}$$

to do the series of Taylor, it has to be taken into account the characteristic length of the element $h^{(e)}$ in the space. Consequently, and starting for the first term of the equation

$$\begin{aligned}
&-\int_V \frac{1}{\kappa}\frac{\partial p}{\partial t}dV \Rightarrow \\
&-hA\frac{1}{\kappa}\frac{\partial p}{\partial t} = -hA\frac{1}{\kappa}\frac{\partial p}{\partial t} + \frac{h^2A}{2}\frac{d}{dx}\left(\frac{1}{\kappa}\frac{\partial p}{\partial t}\right)
\end{aligned} \tag{21}$$

$$\begin{aligned}
&\int_V \frac{1}{n_f}\frac{\partial n_f}{\partial t}dV \Rightarrow \\
&hA\frac{1}{n_f}\frac{\partial n_f}{\partial t} = hA\frac{1}{n_f}\frac{\partial n_f}{\partial t} - \frac{h^2A}{2}\frac{d}{dx}\left(\frac{1}{n_f}\frac{\partial n_f}{\partial t}\right)
\end{aligned} \tag{22}$$

$$\begin{aligned} \int_V \varepsilon_v dV \Rightarrow \\ hA\varepsilon_v = hA\varepsilon_v - \frac{h^2 A}{2}\frac{d\varepsilon_v}{dx} \end{aligned} \tag{23}$$

in consequence, the mass balance equation is defined in the following way

$$\begin{aligned} -hA\frac{1}{\kappa}\frac{\partial p}{\partial t} + \frac{h^2 A}{2}\frac{d}{dx}\left(\frac{1}{\kappa}\frac{\partial p}{\partial t}\right) + hA\frac{1}{n_f}\frac{\partial n_f}{\partial t} - \frac{h^2 A}{2}\frac{d}{dx}\left(\frac{1}{n_f}\frac{\partial n_f}{\partial t}\right) + hA\varepsilon_v - \frac{h^2 A}{2}\frac{d\varepsilon_v}{dx} \Rightarrow \\ \frac{1}{\kappa}\frac{\partial p}{\partial t} - \frac{1}{n_f}\frac{\partial n_f}{\partial t} - \varepsilon_v - \frac{h}{2}\frac{d}{dx}\left(\frac{1}{\kappa}\frac{\partial p}{\partial t} - \frac{1}{n_f}\frac{\partial n_f}{\partial t} - \varepsilon\right) = 0 \end{aligned} \tag{24}$$

the expression (24) is the mass balance equation after application of the Taylor series, it has to be remarked that the expression hA disappears. If $r_v := \frac{1}{\kappa}\frac{\partial p}{\partial t} - \frac{1}{n_f}\frac{\partial n_f}{\partial t} - \varepsilon_v$ is considered, the final equation would be

$$r_v - \frac{h}{2}\frac{dr_v}{dx} = 0 \tag{25}$$

with regard to the linear momentum conservation expression, the same procedure as in the case of the aforementioned equation is done, then, the linear momentum conservation in its global form is

$$\int_V \rho\frac{\partial v_i}{\partial t}dV - \int_V \frac{\partial \sigma_{ij}}{\partial x_j}dV - \int_V \left(b_i - \frac{1}{n_f}f_i^{pf}\right)dV = 0 \tag{26}$$

in the same way as in the mass balance equation, it will be applied the series of Taylor in each term separately

$$\begin{aligned} \int_V \rho\frac{\partial v_i}{\partial t}dV \Rightarrow \\ hA\rho\frac{\partial v_i}{\partial t} = hA\rho\frac{\partial v_i}{\partial t} - \frac{h^2 A}{2}\frac{\partial}{\partial x_j}\left(\rho\frac{\partial v_i}{\partial t}\right) \end{aligned} \tag{27}$$

$$\begin{aligned} \int_V \frac{\partial \sigma_{ij}}{\partial x_j}dV \Rightarrow \\ hA\frac{\partial \sigma_{ij}}{\partial x_j} = hA\frac{\partial \sigma_{ij}}{\partial x_j} - \frac{h^2 A}{2}\frac{\partial^2 \sigma_{ij}}{\partial^2 x_j} \end{aligned} \tag{28}$$

$$\begin{aligned} \int_V \left(b_i - \frac{1}{n_f}f_i^{pf}\right)dV \Rightarrow \\ hA\left(b_i - \frac{1}{n_f}f_i^{pf}\right) = hA\left(b_i - \frac{1}{n_f}f_i^{pf}\right) - \frac{h^2 A}{2}\frac{\partial}{\partial x_j}\left(b_i - \frac{1}{n_f}f_i^{pf}\right) \end{aligned} \tag{29}$$

substituting the expressions (27), (28) and (29) in equation (26), the final form of the linear momentum balance equation will be obtained

$$\begin{aligned} hA\rho\frac{\partial v_i}{\partial t}+\frac{h^2A}{2}\frac{\partial}{\partial x_j}\left(\rho\frac{\partial v_i}{\partial t}\right)-hA\frac{\partial \sigma_{ij}}{\partial x_j}+\frac{h^2A}{2}\frac{\partial^2\sigma_{ij}}{\partial^2 x_j}-hA\left(b_i-\frac{1}{n_f}f_i^{pf}\right) \\ +\frac{h^2A}{2}\frac{\partial}{\partial x_j}\left(b_i-\frac{1}{n_f}f_i^{pf}\right)=0\Rightarrow \\ \rho\frac{\partial v_i}{\partial t}-\frac{\partial \sigma_{ij}}{\partial x_j}-\left(b_i-\frac{1}{n_f}f_i^{pf}\right)-\frac{h}{2}\frac{\partial}{\partial x_j}\left(\rho\frac{\partial v_i}{\partial t}+\frac{\partial \sigma_{ij}}{\partial x_j}+\left(b_i-\frac{1}{n_f}f_i^{pf}\right)\right)=0 \end{aligned} \tag{30}$$

as in equation (24), the expression hA is removed. In the next section, the fluid equation discretized will be shown.

3.1.3 Discretization of the fluid equations

Once the main equations are known, it will proceed with their discretization using a polynomial interpolation with a C_0 approximation using the same shape functions for both, velocities and pressures. To do that, the same shape functions will be considered, hence

$$\mathbf{v}=\mathbf{N}_v\overline{\mathbf{v}},\quad \mathbf{w}=\mathbf{N}_w\overline{\mathbf{w}},\quad \mathbf{q}=\mathbf{N}_q\overline{\mathbf{q}},\quad \mathbf{p}=\mathbf{N}_p\overline{\mathbf{p}} \tag{31}$$

being each of the vectors

$$\begin{aligned} \overline{\mathbf{v}}=\begin{Bmatrix}\mathbf{v}^1\\ \mathbf{v}^2\\ \vdots\\ \mathbf{v}^N\end{Bmatrix}\quad where\quad \mathbf{v}^i=\begin{Bmatrix}v_1^i\\ v_2^i\\ v_3^i\end{Bmatrix},\quad \overline{\mathbf{w}}=\begin{Bmatrix}\mathbf{w}^1\\ \mathbf{w}^2\\ \vdots\\ \mathbf{w}^N\end{Bmatrix}, \\ \overline{\mathbf{q}}=\begin{Bmatrix}\mathbf{q}^1\\ \mathbf{q}^2\\ \vdots\\ \mathbf{q}^N\end{Bmatrix},\quad \overline{\mathbf{p}}=\begin{Bmatrix}\mathbf{p}^1\\ \mathbf{p}^2\\ \vdots\\ \mathbf{p}^N\end{Bmatrix}\quad where\quad \mathbf{p}^i=\begin{Bmatrix}p_1^i\\ p_2^i\\ p_3^i\end{Bmatrix} \\ \mathbf{N}_v=\mathbf{N}_p=\begin{bmatrix}\mathbf{N}_1, & \mathbf{N}_2, & \cdots, & \mathbf{N}_N\end{bmatrix}^T \end{aligned} \tag{32}$$

in (31) the vector $\overline{\mathbf{v}}$ is the global velocity vector for the whole mesh, which contains all velocity vectors of all nodes, $\mathbf{v}^i$ in the velocity vector of the node i and v_j^i is the value of the component j for the velocity vector of the node i. Considering this type of interpolation,

the momentum conservation equation could be defined as

$$\begin{aligned}\int_\Omega N_i \rho N_j d\Omega \dot{\overline{\mathbf{v}}} - \int_\Gamma N_i t d\Gamma + \int_\Omega \nabla N_i N_j d\Omega \overline{\mathbf{p}} \\ + \int_\Omega \nabla N_i 2\mu \left(\varepsilon_{ij} - \frac{1}{3}\varepsilon_v \delta_{ij}\right) d\Omega - \int_\Omega N_i b_i d\Omega - \int_\Omega N_i \frac{1}{n_f} f_i^{pf} d\Omega = 0\end{aligned} \tag{33}$$

while the mass conservation law has the following form

$$\begin{aligned}\int_\Omega N_i \frac{1}{\kappa} N_j d\Omega \dot{\overline{\mathbf{p}}} - \int_\Omega N_i \frac{1}{n_f} \frac{\partial n_f}{\partial t} d\Omega - \int_\Omega N_i \nabla N_j d\Omega \overline{\mathbf{v}} - \int_\Gamma N_i \tau N_j d\Gamma \overline{\mathbf{p}} \\ - \int_\Gamma q\tau \left(\rho \frac{\partial v_n}{\partial t} - \frac{2}{h_n}\epsilon_n - t_n + \frac{1}{n_f} f_i^{pf}\right) d\Gamma + \int_\Omega \nabla N_i \tau \nabla N_j d\Omega \overline{\mathbf{p}} \\ + \int_\Omega \nabla N_i \tau \left(\nabla(2\mu\varepsilon_{ij}) + b_i + \frac{1}{n_f} f_i^{pf}\right) d\Omega = 0\end{aligned} \tag{34}$$

considering the following definitions

$$Mass\ matrix \quad M_{ij} = \int_\Omega N_j \rho N_i d\Omega \tag{35}$$

$$Coupling\ matrix \quad Q_{ij} = \int_\Omega N_j \mathbf{m} N_i d\Omega \tag{36}$$

$$Stiffness\ matrix \quad K_{ij} = \int_\Omega \nabla N_j \mu D \nabla N_i d\Omega \Rightarrow K_{ij} = \int_\Omega B_j \mu D B_i d\Omega \tag{37}$$

where D is the constitutive matrix and B is the deformation matrix which are defined as

$$Deformation\ matrix \quad B_{ij} = \begin{bmatrix} \frac{\partial N_i}{\partial x_1} & 0 & 0 \\ 0 & \frac{\partial N_i}{\partial x_2} & 0 \\ 0 & 0 & \frac{\partial N_i}{\partial x_3} \\ \frac{\partial N_i}{\partial x_2} & \frac{\partial N_i}{\partial x_1} & 0 \\ \frac{\partial N_i}{\partial x_3} & 0 & \frac{\partial N_i}{\partial x_1} \\ 0 & \frac{\partial N_i}{\partial x_3} & \frac{\partial N_i}{\partial x_2} \end{bmatrix} \tag{38}$$

$$Constitutive\ matrix \quad D_{ij} = \begin{bmatrix} 2 & 0 & 0 \\ 0 & 2 & 0 \\ 0 & 0 & 1 \end{bmatrix} \tag{39}$$

$$L_{ij} = \int_{\Omega} \nabla N_i \tau \nabla N_j d\Omega \tag{40}$$

$$M_{b_{ij}} = \int_{\Gamma} N_i \tau N_j d\Gamma \tag{41}$$

$$M_{1_{ij}} = \int_{\Gamma} N_i \frac{1}{\kappa} N_j d\Gamma \tag{42}$$

the force vector, in the case of the linear momentum conservation law equation is

$$f_{vl} = \int_{\Gamma} N_i t d\Gamma + \int_{\Omega} \nabla N_i 2\mu \left(\varepsilon_{ij} - \frac{1}{3} \varepsilon_v \delta_{ij} \right) d\Omega - \int_{\Omega} N_i b_i d\Omega \tag{43}$$

whereas the aforementioned vector in the case of the mass conservation law is defined as follows

$$\begin{aligned} f_{pl} = \int_{\Omega} N_i \frac{1}{n_f} \frac{\partial n_f}{\partial t} d\Omega + \int_{\Gamma} q\tau \left(\rho \frac{\partial v_n}{\partial t} - \frac{2}{h_n} \epsilon_n - t_n + \frac{1}{n_f} f_i^{pf} \right) d\Gamma + \\ \int_{\Omega} \nabla N_i \tau \left(\nabla (2\mu \varepsilon_{ij}) + b_i + \frac{1}{n_f} f_i^{pf} \right) d\Omega \end{aligned} \tag{44}$$

thus, from the definitions mentioned above, it can be obtained

$$M\dot{\overline{\mathbf{v}}} + K\overline{\mathbf{v}} + Q\overline{\mathbf{p}} - f_{vl} = 0 \tag{45}$$

$$M_1\dot{\overline{\mathbf{p}}} - Q\overline{\mathbf{v}} + (L + M_b)\overline{\mathbf{p}} - f_{pl} = 0 \tag{46}$$

for the resolutions of the equations (45) and (46), the implicit Newton-Rhaphson will be used. To solve (45) the following expression has to be defined

$$A \cdot x = b \tag{47}$$

taking into account the Lagrangian approach, it can be satisfied that

$$\dot{\mathbf{v}} = \frac{\partial v}{\partial t} = \frac{^{n+1}v - {}^{n}v}{\Delta t} \tag{48}$$

and setting the following relations

$$x = \Delta\dot{\mathbf{v}}, \quad A = \frac{M_o}{\Delta t} + K + K_v = H_v \quad and \quad b = -r_{mi} \tag{49}$$

the final equation to solve would be

$$^{n+1}H_v\Delta\overline{\mathbf{v}} = -^{n+1}\overline{\mathbf{r}}_m^k \tag{50}$$

It is worth to highlight that K_v is known as *"bulk" stiffness matrix*, a stiffness matrix that it takes into account the changes in pressure due to velocity [23]. Its use has been proven critical to maintain the mass, a fast convergence and a good accuracy. Its computation can be found in the Appendix B of [23]

$$K_v = \int_\Omega \mathbf{B}^T\mathbf{m}\theta\Delta t\kappa\mathbf{m}^T\mathbf{B}d\Omega \tag{51}$$

3.1.4 Two step velocity-pressure strategy

In this work, the two step v-p (velocity-pressure) strategy has been regarded to verify examples. This strategy, developed in [23] solves iteratively the fluid system of equations in two steps, the first one is the linear momentum equation with the objective to compute the increment of the nodal velocity $\Delta\bar{v}$ and the mass balance equation for the nodal pressures $\bar{p}$. After computing the fluid equations, the following step is to remesh the continuum domain.

When the quality mesh is checked and the remesh is produced, the following step is to solve the equation (45). Then, the kinematics have to be updated ($\bar{x}_{i+1}^{n+1}$, $\bar{u}_{i+1}^{n+1}$ and $\bar{\dot{u}}_{i+1}^{n+1}$) and the same has to be done for the case of the forces $F_{p,i+1}^{n+1}$. Once the forces are updated, it is posible to solve the equation (46) with the purpose of obtaining the new pressure. After that, $\bar{u}_{i+1}^{n+1}$ and $\bar{p}_{i+1}^{n+1}$ are used to update the Cauchy stress tensor and finally, σ_{i+1}^{n+1} and $\bar{\dot{u}}_{i+1}^{n+1}$ let us update the residual $(\overline{\mathbf{r}}_m)_{i+1}^{n+1}$.

3.1.5 Remeshing process

Due to the movement of nodes, large deformations in the mesh are produced leading to the deterioration of discretization. For this reason, the quality of the mesh is checked at the beginning of each time step. If the distortion is over a threshold previously imposed, the mesh would be deleted and discretization would be built again.

This process which is called remesh procedure is the principal characteristic of PFEM. When the mesh is distorted, all the elements are removed and all information is stored in the nodes. The new mesh is generated using a Delaunay triangulation [26] which, given a set of points, draws the Voronoi polygons and, after that, circumferences whose center is each of the Voronoi vertex. The Delaunay triangulation matches every node that is on the

circumference created. In Figure 2 can be seen the process.

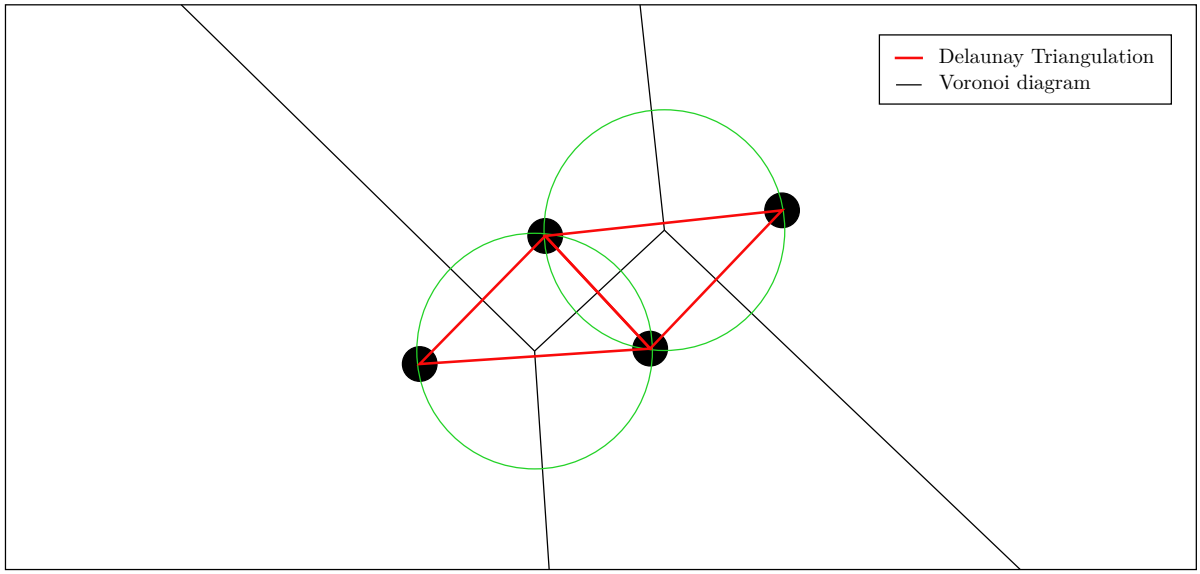

Figure 2: Delaunay triangulation process

The problem with this triangulation is that it does not distinguish the isolated nodes, as a consequence, it creates distorted elements which make it difficult to obtain reasonable results. For this reason, the so-called Alpha Shape method is used [27]. This method removes the elements which do not satisfy the following relation

$$R \leq \alpha h \tag{52}$$

where R is the circumradius, h is the characteristic mesh size. In the present work, the alpha parameter will be set in 1.3. In the Figure 3, the process of remeshing is shown.

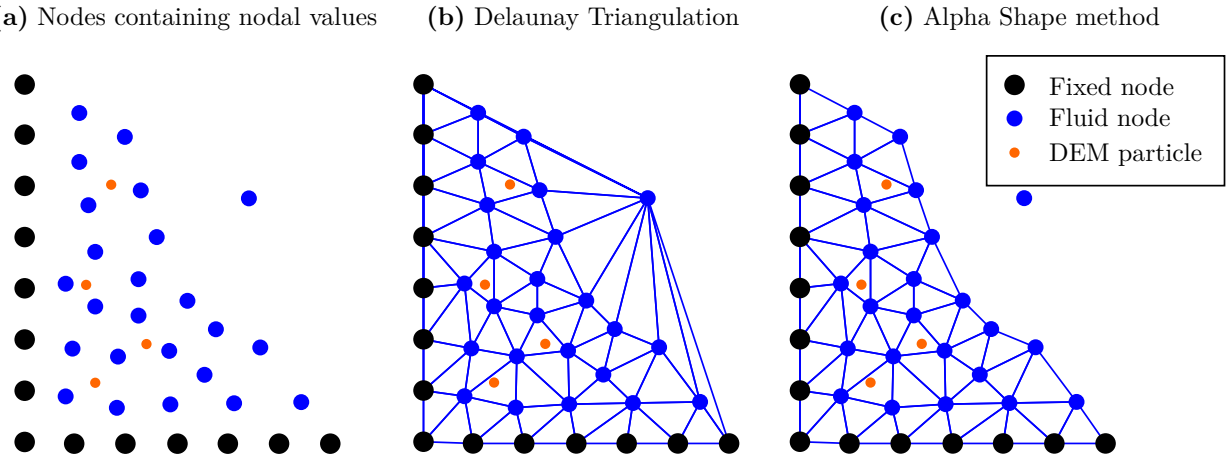

Figure 3: Remeshing process including DEM particles

Due to the remeshing process at each time step, there can be a concentration of nodes in a small region producing distorted elements, to avoid that, the nodes can be removed and

added in other place inside the domain. The value of the nodal variables in the new node is obtained by interpolation of the values in the neighboring nodes.

3.2 DEM formulation

In the present section, the formulation for the solid particles is shown. First of all, it has to be taken into account that the movement of a solid particle can be described by means of the solid rigid dynamic equations. There are two types so, for a particle i

$$m_i \ddot{u}_i = F_i \tag{53}$$

$$I_i \dot{w}_i = T_i \tag{54}$$

Where u_i is the displacement in the center of the particle in X, w_i the angular velocity, m_i the particle mass, I_i the moment of inertia, F_i the resultant force and T_i the resultant moment over the central axis. Hence, these last terms can be decomposed as

$$F_i = F_B + F_{hydro} + \sum_{k_{pn}} F_{k_{pn}} + \sum_{k_{wn}} F_{k_{wn}} =: F \tag{55}$$

$$T_i = T_{hydro} + T_{contact} \tag{56}$$

F_B is the buoyancy force, for this work, it has been considered the Archimedes Buoyancy Law which has the following expression

$$F_B = (m_p - m_f)\mathbf{g} \tag{57}$$

In the previous equation m_p is the mass of the particle while m_f is the mass of the fluid which is displaced by the particle. F_{hydro} is the hydrodynamic force that represents the relative displacement of the particle with respect to the fluid surrounding it. It has the following expression

$$F_{hydro} = F_U + F_A + F_D \tag{58}$$

In equation(58), F_U is the force that computes the displaced that fluid suffers when it interacts with the particle. It is defined as follows

$$F_U = m_f \frac{\partial u}{\partial t} \tag{59}$$

This equation can be maintained for a wide range of Reynolds number value, as it is confirmed in [28], who simulated the motion of bubbles, particles considering the effects of the finite Reynolds number. The following term in (58) is the added mass force F_A which is the resistance that the fluid has to be moved by the particle

$$F_A = \frac{1}{2} m_f \left(\frac{\partial u}{\partial t} - \frac{dv}{dt} \right) \tag{60}$$

As (59), the added mass force is robust and generally applicable to any Reynods number. Wakaba *et al.* [29] showed that same results can be obtained for the drag coefficient varying the acceleration number and the added mass coefficient for a huge range of Reynolds number.

Finally, the last summand in being regarded for expression (58) is the drag force. It can be defined as averaged force by a submerged particle in a stationary flow. The direction of the flow will be the one resulted by the direction of the relative velocity between the particle and the far field. It is defined in the following equation

$$F_D = \frac{1}{2}\mu_p A_p C_D ||\mathbf{w}||(\mathbf{w}) \tag{61}$$

μ_p is the density of the particle, A_p is the cross sectional area for a orthogonal section to $\mathbf{w} := \mathbf{u} - \mathbf{v}$ and C_D is the drag coefficient. The drag law coefficient is strongly dependent on particle based Reynolds number which is defined by the following equation

$$Re_p = \frac{d_p|\mathbf{w}|}{v_f} \tag{62}$$

Where d_p is the diameter of the particle and v_f is the kinematic viscosity of the fluid. To compute the coefficient, the Schiller and Naumann law is considered [30]. This law lets to compute correctly the drag coefficient for any Reynolds number which means that this law is a generalization of Stokes. This generalization is set in the following expression

$$C_D(Re_p) = \begin{cases} (1 + 0.15Re_p^{0.687})C_{D,Stokes} & \text{if } Re_p \leq 1000 \\ 0.44 & \text{otherwise} \end{cases} \tag{63}$$

To compute the solid particles, firstly, the displacement of them is computed. After that and with the purpose of knowing if there is interaction between particles, the neighbors of them are search. As this operation is computationally expensive is not taken account in every time step so it is assume that, if a particle j is the neighbor of another i it will remain as a neighbor in the following step.

Searching consists in describing, for a particle, a circumference of a given radius with its center in the center of the solid particle and to analyse what discrete elements are in the interior of the mentioned circumference which will be the neighbors. The process is described in the Figure 4.

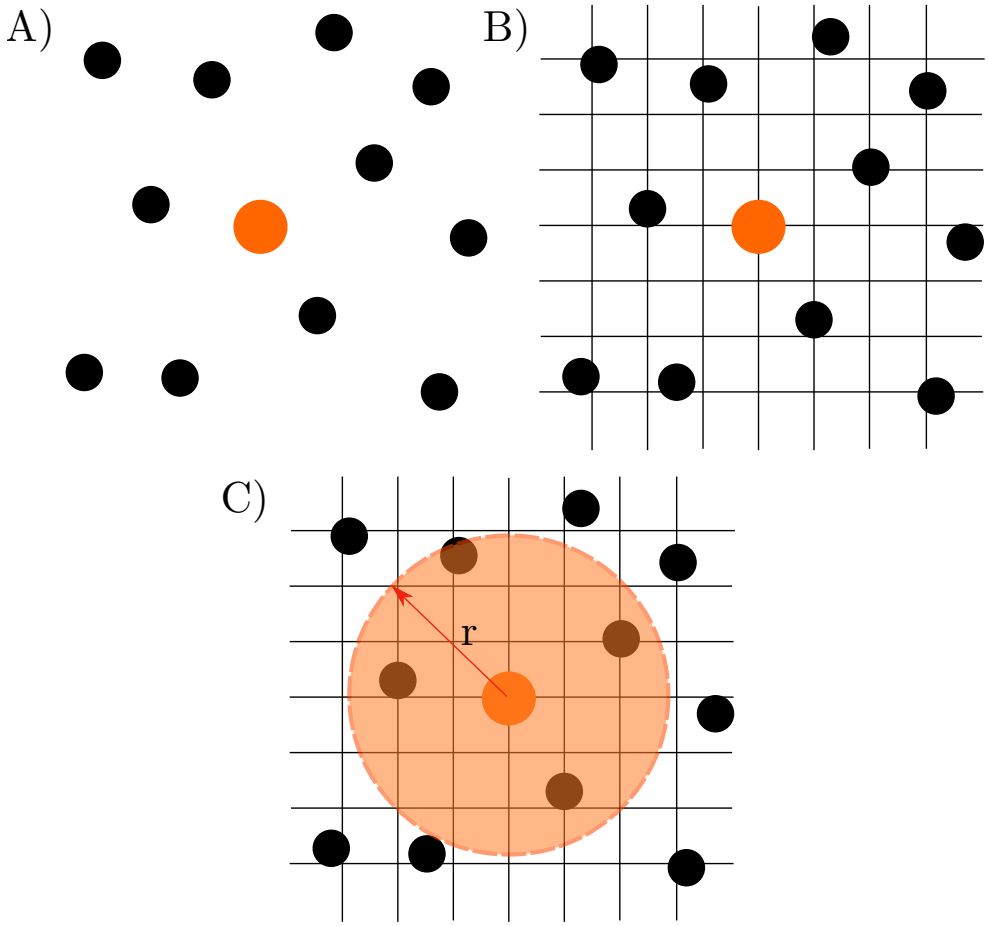

Figure 4: Neighboring process

Once search is done, the next step is to calculate the external forces, in this work, these will be the forces resulting from the interaction between the fluid and the particle. The last forces to calculate are the contact between the particles and between the particles and rigid walls. These forces are based on the Hertz contact model with the friction of Coulomb and a viscous damper detailed in [31].

Finally, to update the the position and velocity of each particle, the integration scheme chosen is Symplectic Euler [32]. In this scheme, it is used the velocity in the current configuration to compute the new value and the updated velocity to compute the position in the next configuration. This scheme can be defined as

$$v_{p,m+1} = v_{p,m} + \Delta t_{DEM} \frac{\mathbf{f}_{p,m}}{m_p} \tag{64}$$

$$x_{p,m+1} = x_{p,m} + \Delta t_{DEM} v_{p,m+1} \tag{65}$$

Where m is the current configuration and $m+1$ the updated one and $\mathbf{f}_{p,m}$ is the second order time derivative of the particle's position.

3.3 PFEM-DEM coupling

In the previous sections, the formulation used to model the Lagrangian fluids and the solid particles has been introduced. In this section, the way to couple both phases will be described in detail. For PFEM-DEM coupling, there exists two different types

1. One way coupling. In this case, the fluid solution affects to the motion of the particles but the movement of them does not affect to the fluid (*forward coupling*).
2. Two way coupling. The fluid solution is also considered to compute the movement of the particles (*forward coupling*), but, in this case, the particles solution affects to the fluid motion (*backward coupling*).

In this thesis, the so-called (*updated fluid*) strategy has been applied only for one way coupling, the another type has not been used. To use the strategy selected, the fluid solution is computed first. Then, the value of the fluid variables are determined in the position of the particles. To do that, it is necessary to find what fluid elements are relevant to compute the motion of the particles with the purpose of computing the variables involved in the coupling from those elements.

To search the mentioned elements, a bin data structure has been used as detailed in [33]. As mentioned before, the search procedure is not used in every time step, so this bin is created in the steps in which the neighboring is done. When the particles are located in the mesh, the fluid data at their positions $\mathbf{x}_P$ have to be obtained. Hence, the velocity of a particle $u_i(\mathbf{x}_P)$ is

$$u_i(\mathbf{x}_P) = N^{bn}(\mathbf{x}_P)\bar{\mathbf{u}}_i^{bn} \tag{66}$$

Where $N^{bn}(\mathbf{x}_P)$ is the linear shape function evaluated at the position of the particle P and bn ranges from 0 to the number of nodes of the fluid element that contains the particle.

It is important to remark that two way coupling of the type *weak* means that the fluid fraction and fluid fraction rate are not considered. In one way coupling they are neither considered.

4 Validation examples

In this section three tests will be studied whose purpose is to compare the solution obtained with the ones provided in the literature. The first one is the evaluation of the sedimentation of a particle in a fluid at rest. The final velocity of the particle will be compared with the analytical one provided by Stokes drag law.

The second one will consist in a water dam break with six particles embedded in a fluid continuum. This case will be compared with experimental results to validate the fluid phase with [34].

Finally, the third test is a water discharge from a prismatic tank. This one will be used to compare the movement of the fluid with the known analytical solution. Due to the fact that in one simulation the particles' density will be the same as the fluid one, DEM can be used as tracers of the fluid streamlines. Those tests are described and performed from [35].

4.1 Sedimentation of a sphere in a fluid at rest

The test carried out in this section has been used widely to test the CFD DEM solvers [36]. The particle falls due to the graphic and, because the fluid is at rest, the number of particle Reynolds is small so the standard Stoke's Law can be used providing a good accuracy. As in [36], the temporal evolution of the particle vertical velocity can be obtained using the following expression:

$$v_y = \frac{gV_p(\rho_p - \rho_f)}{3\pi\mu_f d_p}\left(1 - e^{\frac{-3\pi\mu_f d_p t}{V_p \rho_p}}\right) \tag{67}$$

where $g = 9.81 m/s^2$ is the gravity acceleration, V_p id the volume of the spherical particle, $\rho_p = 2500 kg/m^3$ and $\rho_f = 1500 kg/m^3$ are the particles and fluid densities, $\mu_f = 0.001 Pa \cdot s$ is the water viscosity and $d_p = 0.1 mm$ is the particle diameter. To compute this formula, it has to be assumed that the hydrodynamic force is the same as the drag one. The representation of the geometry is displayed in Figure 5, in it, a solid particle in the center of a cylindrical tank is placed.

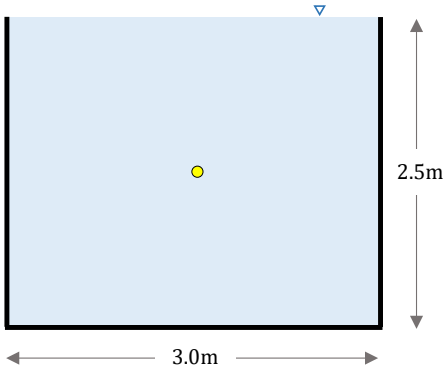

Figure 5: Geometry of the tank and initial position of the particle (size of it is exaggerated to improve the visualization)

As the hydrostatic state is needed to perform the simulation and PFEM fluid needs some time steps to reach it, the particles does not move at the beginning of the model. When the velocity of the fluid is almost null, the DEM particle starts to be considered in the simulation letting it to fall freely. This moment is considered as t = 0.

Finally, the evolution of the velocity obtained using the proposed approach and the one provided by (67) is shown in the Figure 6. As it can be seen, there is a good agreement between both, the numerical and analytical predictions which means that PFEM DEM approach keeps this benchmark test used for CFD DEM solvers.

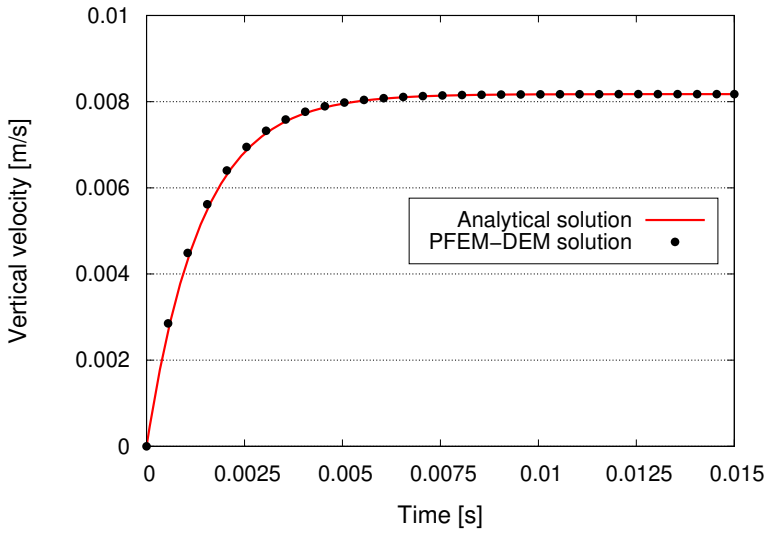

Figure 6: Comparison between the analytical and numerical solution

4.2 Water dam break with embedded particles

This test has been used widely to validate free surface solvers from the experimental results [37]. In this section it is used to validate the PFEM-DEM two step v-p solver strategy for the Lagrangian approach. The original experiment consisted in the removal of a vertical rigid wall so the initial water column collapses. The fluid and the mesh properties are resumed in the next table:

Density $[kg/m^3]$	1000
Bulk modulus [Pa]	$2.1 \cdot 10^9$
Viscosity [Pa s]	0.001
Number of tetrahedra	753303
Mean mesh size [mm]	4.63

Table 1: Initial geometry and fluid properties

The geometry of the water dam break can be seen in Figure 7:

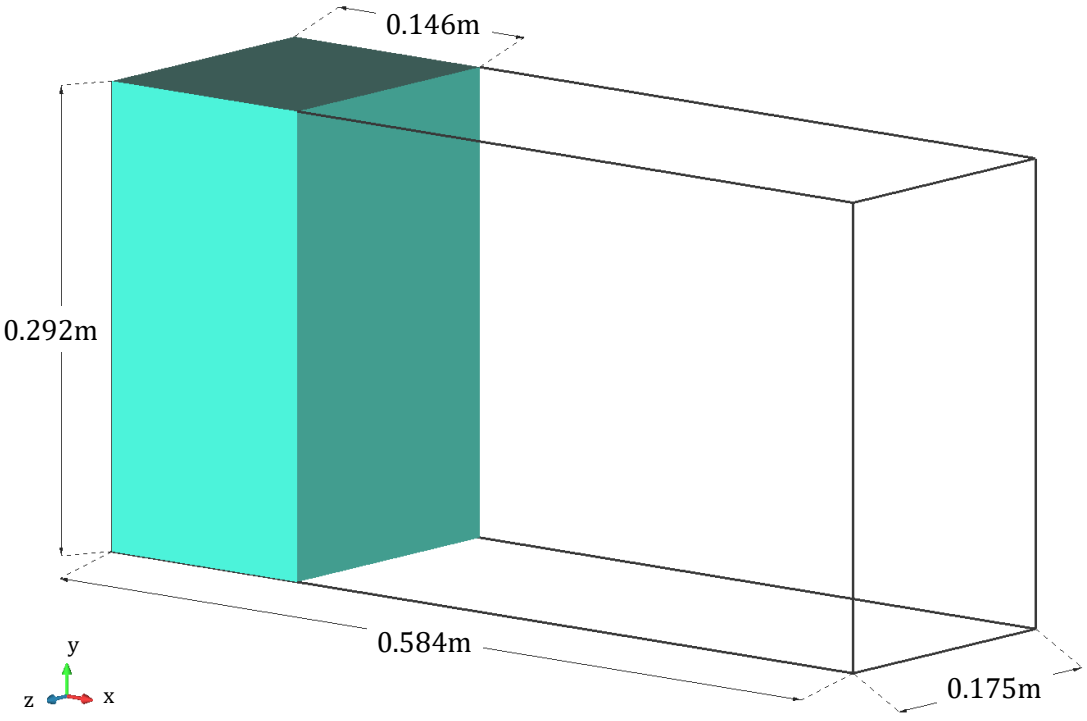

Figure 7: Initial geometry of the water column

Although in the initial experiment, only the fluid phase was measured, in the present document six particles will be considered to analyse how they are settled on the bottom of the container in which the water is stored. The particles have a constant radius $r_p = 0.75mm$ and a density $\rho_p = 1500kg/m^3$. Their initial position are given in the following table:

Particle	x [m]	y [m]	z [m]
A	0.030	0.280	0.0885
B	0.116	0.280	0.0885
C	0.030	0.200	0.0885
D	0.116	0.200	0.0885
E	0.030	0.120	0.0885
F	0.116	0.120	0.0885

Table 2: Initial position of DEM particles

For a better understanding, the position of these particles are displayed in Figure 8 as well:

Figure 8: Position of the particles at the beginning of the simulation

The variables considered for the measurements will be dimensionless and they are defined by the following expressions

$$x^* = x/d \tag{68}$$

$$y^* = y/d \tag{69}$$

$$t^* = t(2g/d)^{0.5} \tag{70}$$

where x is the horizontal coordinate ($x = 0.146$ at the beginning of the test for the fluid front), d is the base of the water column front at the beginning of the simulation so it has a value of $d = 0.146m$, y is the vertical coordinate which is always zero for the fluid front and g is the gravitational acceleration.

In this simulation the displacement of the fluid front will be measured to validate the test. Due to the fact that one-way coupling is used, the embedded particles will not affect to the fluid solution. Therefore, it is expected that the results for the fluid displacement should be similar as the real experiment.

This displacement is compared with the real experiment and other numerical tests [38], [39], [37] and [34] from the beginning to the time before the impact of water with the rigid wall in the opposite side of the container. In Figure 9 can be seen the evolution og the displacement.

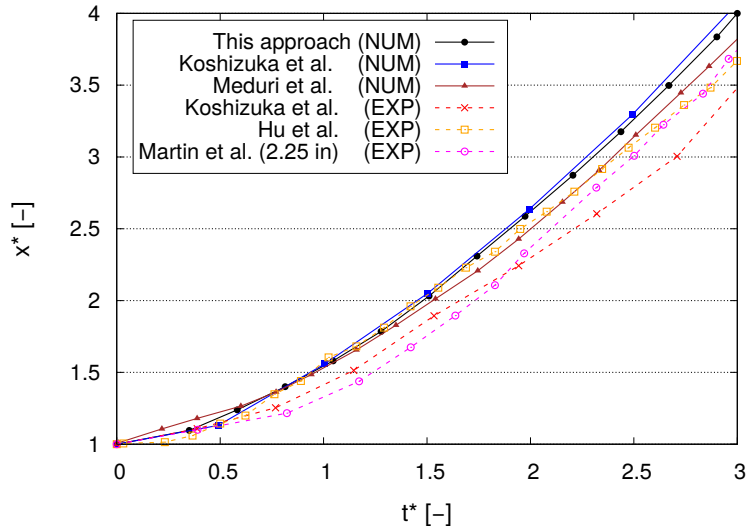

Figure 9: Displacement results for the wave front in comparison with the experimental results and other numerical simulations

In Figure 9, the evolution in dimensionless time of the position is studied, in it, the numerical simulations tend to overestimate the advance of the water column. It may be produced because the rigid wall that maintain the initial column water is removed instantaneously in the experiments while in the simulations, it is removed slowly so the bottom part of the column increases its velocity at the initial time steps.

Another comparison with the experimental results have been done in a qualitative way, in this case, the results are compared from the beginning to the end of the simulation, after the impact with the rigid wall. This can be seen in figures 10-21:

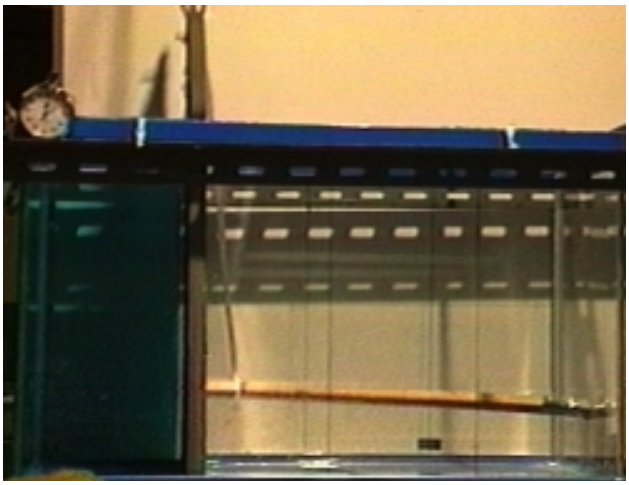

Figure 10: Experiment t = 0s

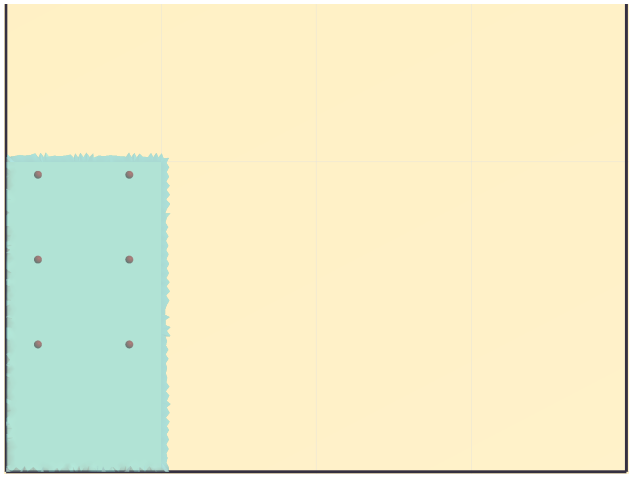

Figure 11: Numerical simulation t = 0s

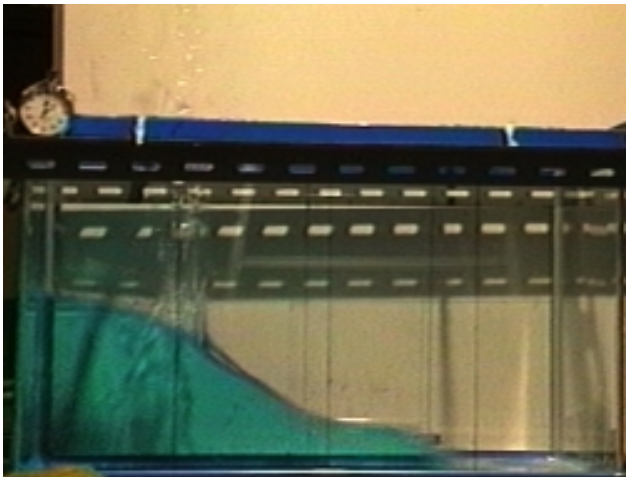

Figure 12: Experiment t = 0.2s

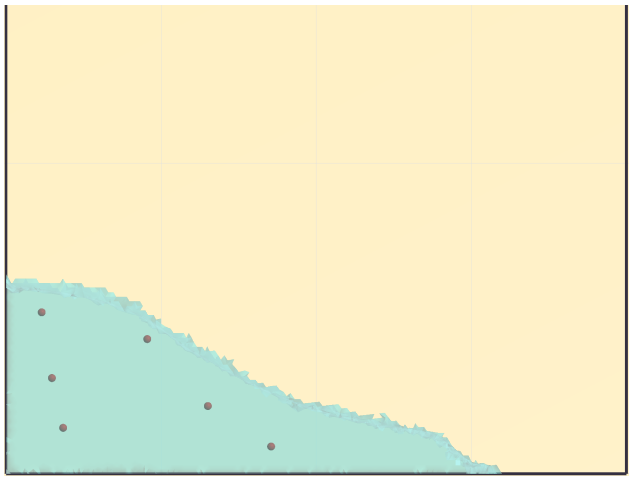

Figure 13: Numerical simulation t = 0.2s

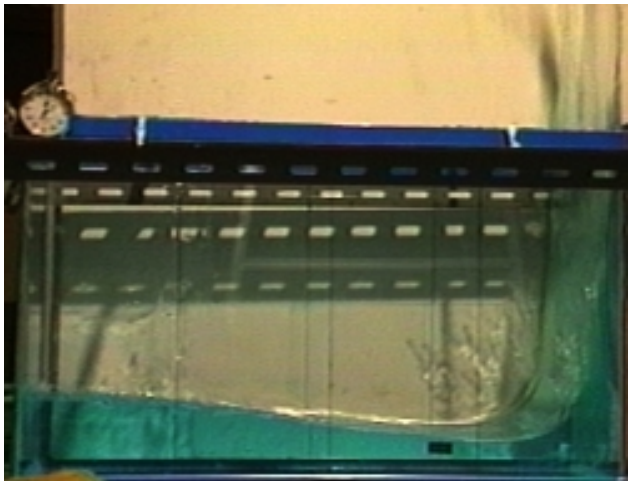

Figure 14: Experiment t = 0.4s

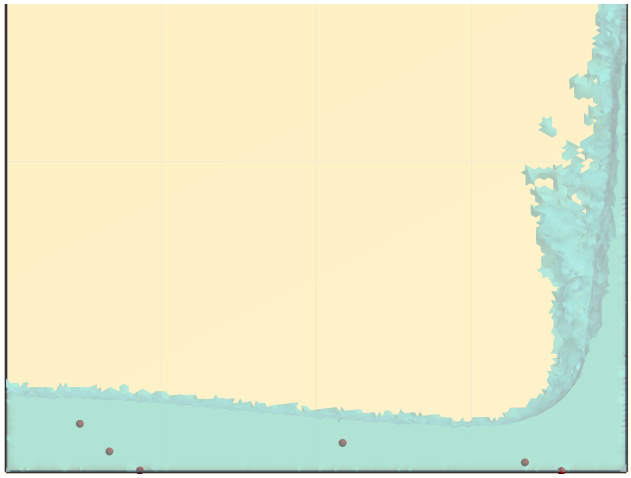

Figure 15: Numerical simulation t = 0.4s

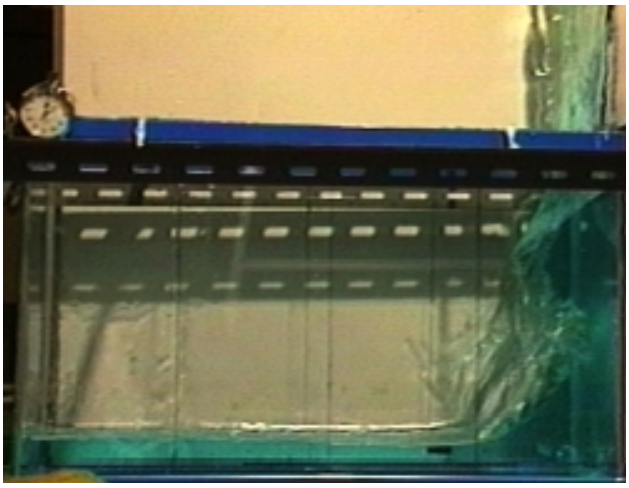

Figure 16: Experiment t = 0.6s

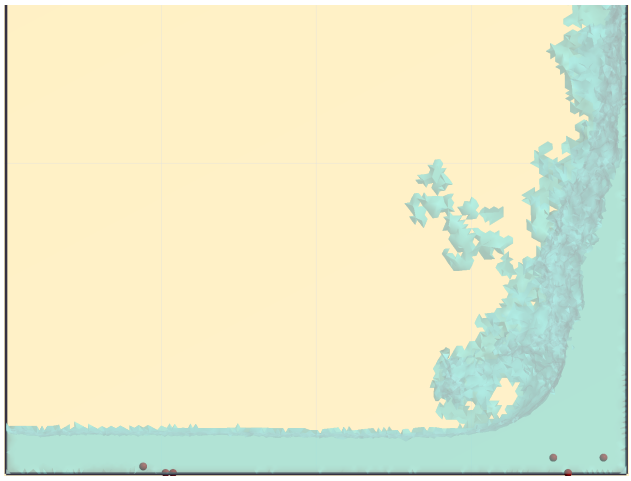

Figure 17: Numerical simulation t = 0.6s

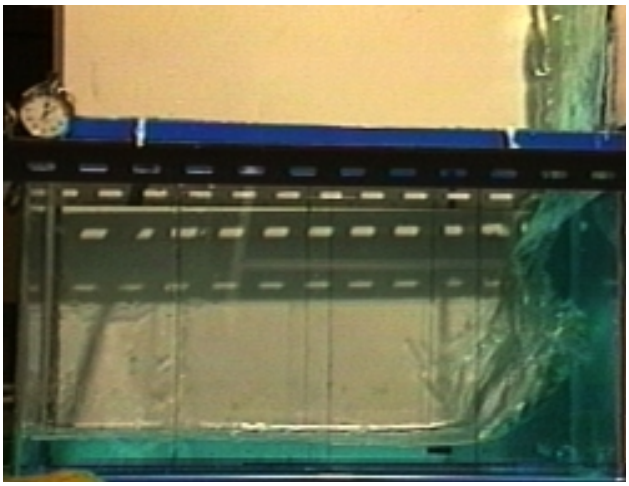

Figure 18: Experiment t = 0.8s

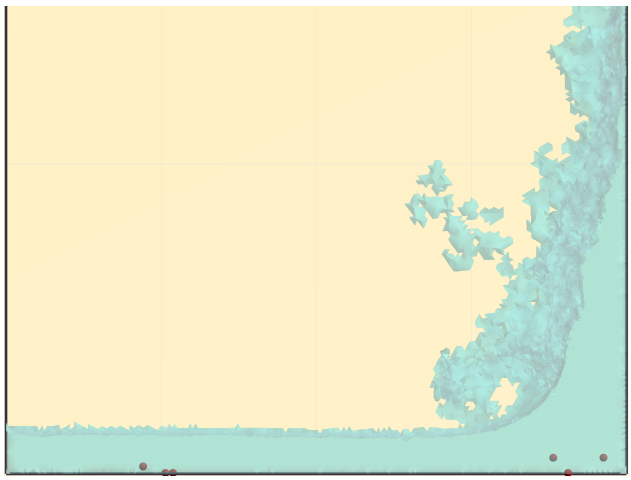

Figure 19: Numerical simulation t = 0.8s

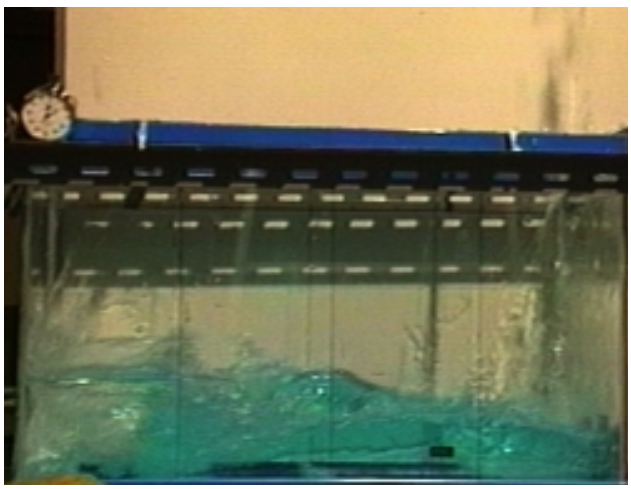

Figure 20: Experiment t = 1s

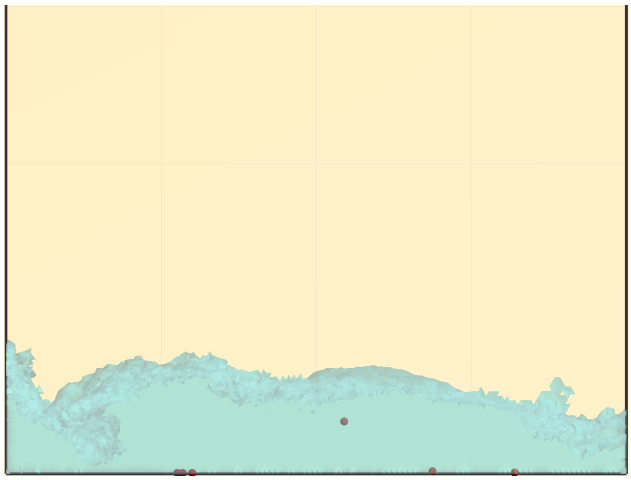

Figure 21: Numerical simulation t = 1s

As it can be seen in the set of images above, it can be concluded that the results obtained are similar to the experiment. However some differences can be detected specially at time step t = 0.2s. Before water reaches the rigid wall, the numerical simulation produces higher velocities in the layer closest to the rigid wall at the bottom of the container.

In terms of velocities, in the following figures 22-24, the dimensionless time evolution of the modulus velocity field before the impact of the wave front is displayed:

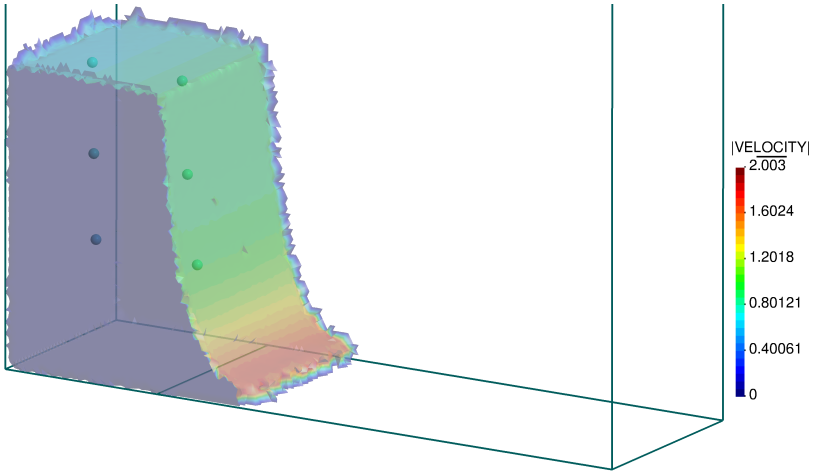

Figure 22: Modulus velocity field at $t^* = 1.05$s

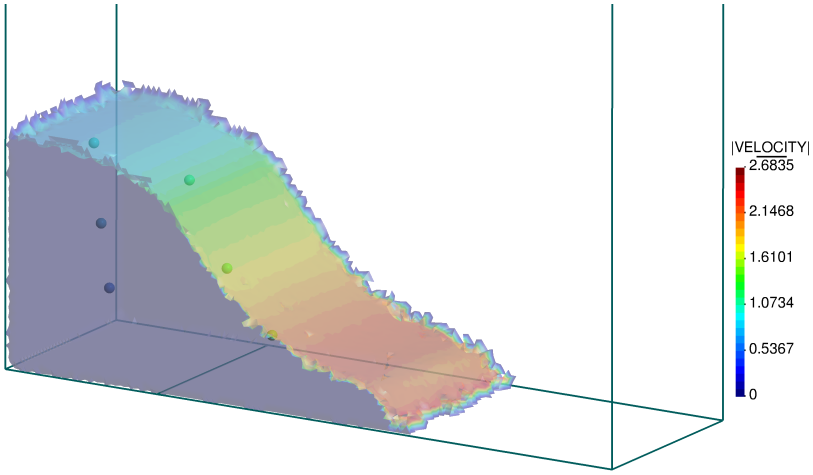

Figure 23: Modulus velocity field at $t^* = 1.97$s

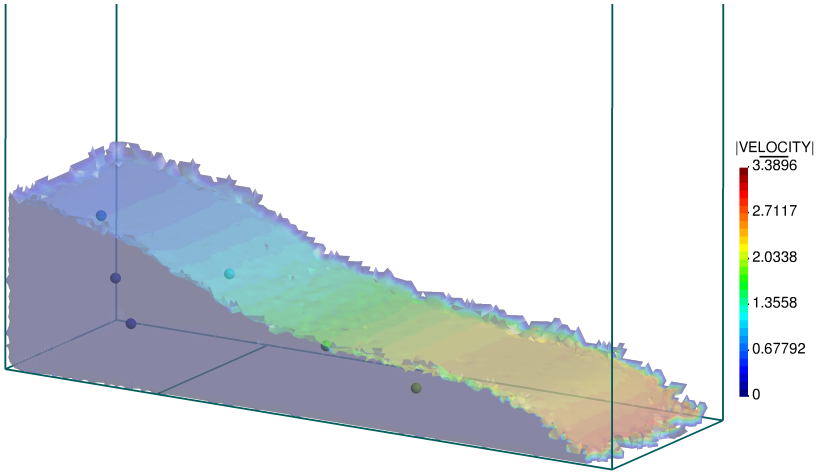

Figure 24: Modulus velocity field at $t^* = 2.90$s

In the figures shown, the particles are represented with a higher volume for a clear visualization of them. In the figures can be seen the conditions in the contact with the rigid surface. The stick conditions used here impose "*null*" velocity for both, the direction of the normals of the rigid surface and the direction perpendicular to them for the nodes in contact with the walls, which explains why the modulus of the velocity is 0 in the surroundings.

Finally, the evolution of particles' position is displayed in figures 25 and 26 as follows:

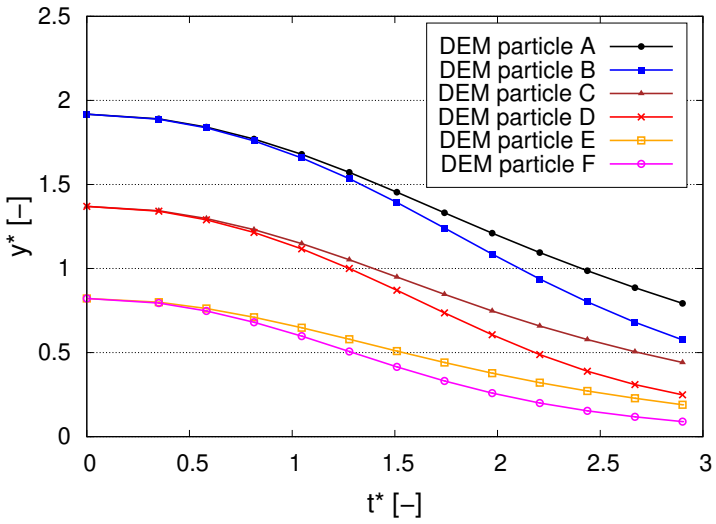

Figure 25: Evolution of the vertical position for the particles

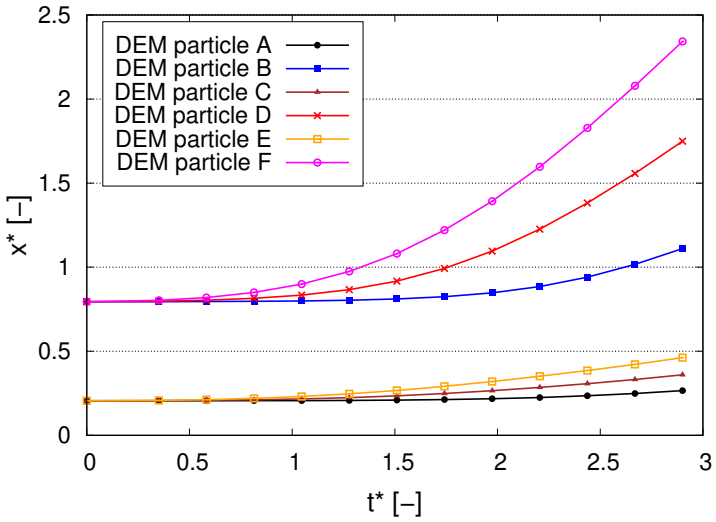

Figure 26: Evolution of the horizontal position for the particles

In the case of the Figure 26 the particles located near to the front suffer a higher displacement than the ones placed close to the rigid surface, which is coherent due to the fact that the higher fluid velocities are reached in the free surface. In Figure 25, as it is reasonable, the particles placed above experiment higher vertical movements than the ones located below. For particles with the same vertical positions, for the same reason explained before, the ones near to the free surface move more than the ones closer to the rigid wall. This last analysis was carried out with the objective of being used to compare with future numerical simulations or experiments.

4.3 Tank discharge

In this test, a discharge of a tank plenty of water and a group of particles will be simulated. This tank is a prismatic one with a circular hole in the center of the bottom with a diameter $D = 0.2m$. The fluid is water with a density $\rho_f = 1000kg/m^3$ and a viscosity $\mu_f = 0.001Pa{\cdot}s$ and it fills the tank entirely at the beginning of the test. The particles are placed creating a cylinder of height $0.5D$ and diameter $0.35m$. This cylinder is formed by 2552 particles of diameter $d_p = 0.005m$ irregularly distributed. The size of the particles and their dispersion leads to consider that they do not affect the fluid solution. Thus, the usage of one way should not distort the solution to be validated. The geometry of the tank is displayed in the figures 27 and 28 as follows:

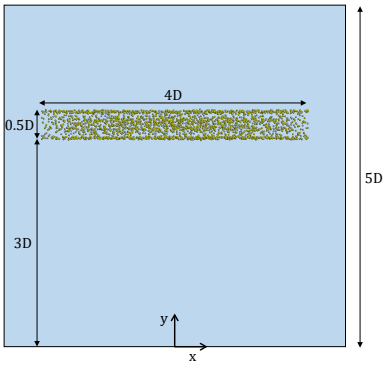

Figure 27: Lateral view of the tank

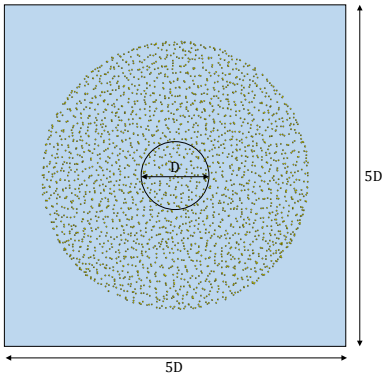

Figure 28: Top view of the water tank

This problem is studied varying the density of the particles which will be $\rho_p = 1000kg/m^3$, $\rho_p = 1125kg/m^3$ and $\rho_p = 1500kg/m^3$. It is important to remark that for the first case, it is expected that the particles behave as tracers of the fluid streamlines. The solution to be measured is the motion of the particle located at $y = 0.65$. The fluid mesh will be formed by 879209 tetrahedral elements with a mean size equal to $h = 0.0225m$. The following dimensionless variables will be evaluated

$$y^* = y/D \tag{71}$$

$$v^* = abs(v_y)/(2gH)^{0.5} \tag{72}$$

$$t^* = t(2gH)^{0.5}/D \tag{73}$$

$$\rho^* = \rho_p/\rho_f \tag{74}$$

$$M^* = M_f/M_{fi} \tag{75}$$

where y^*, v^*, t^*, ρ^* and M^* are the dimensionless vertical coordinate, velocity, time, particle density and water mass, respectively. In addition, the initial free surface level is $H = 1m$,

the gravitational acceleration is $g = 9.81m/s^2$, M_f is the mass water contained in the tank at every time step and M_{fi} is its initial value ($M_{fi} = 1000kg$). In the following sequence of figures 29-40, the results of six time steps for $\rho^* = 1.125$:

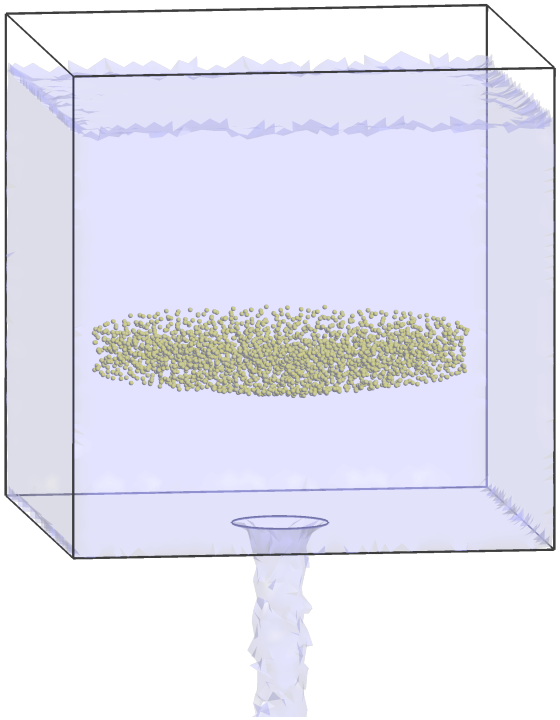

Figure 29: 3D view $t^* = 33.2$

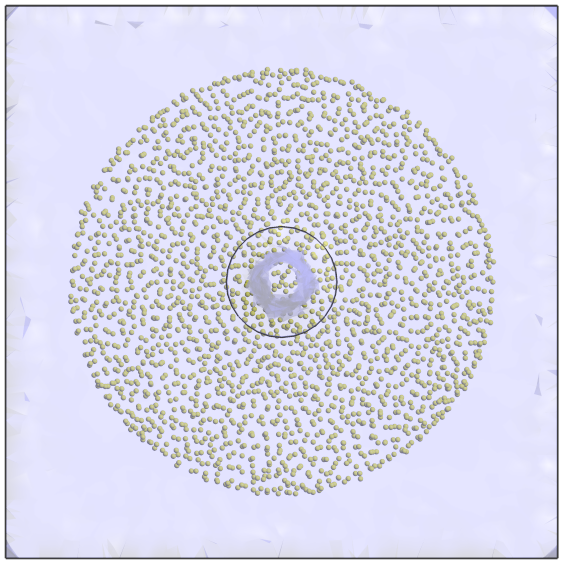

Figure 30: Top view $t^* = 33.2$

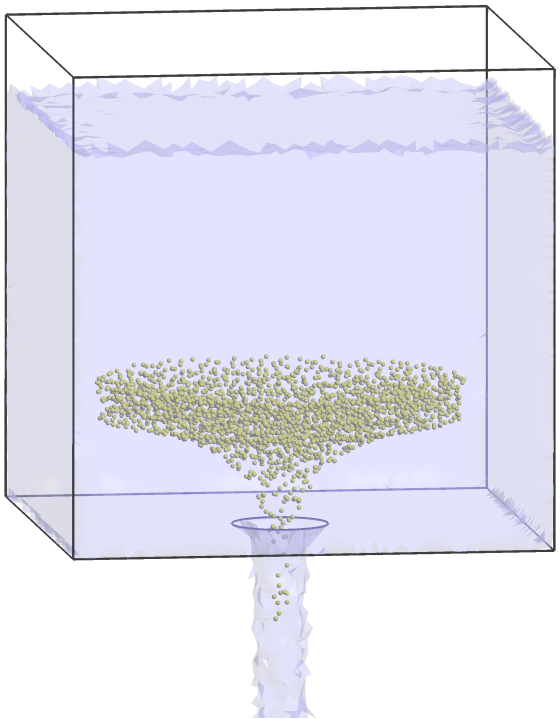

Figure 31: 3D view $t^* = 44.3$

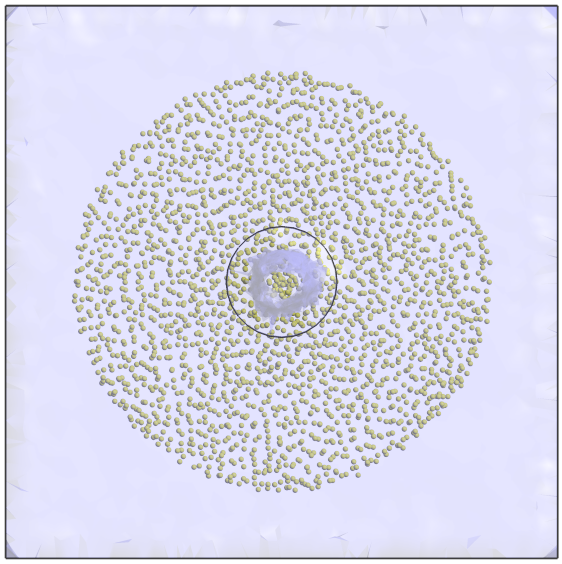

Figure 32: Top view $t^* = 44.3$

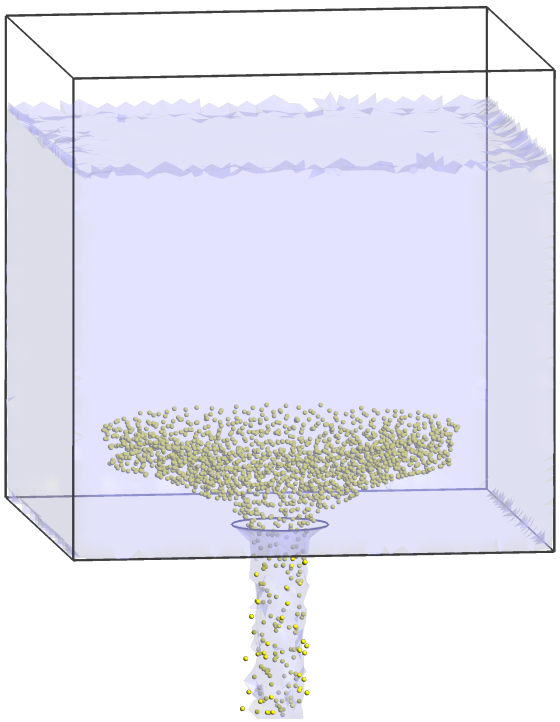

Figure 33: 3D view $t^* = 55.4$

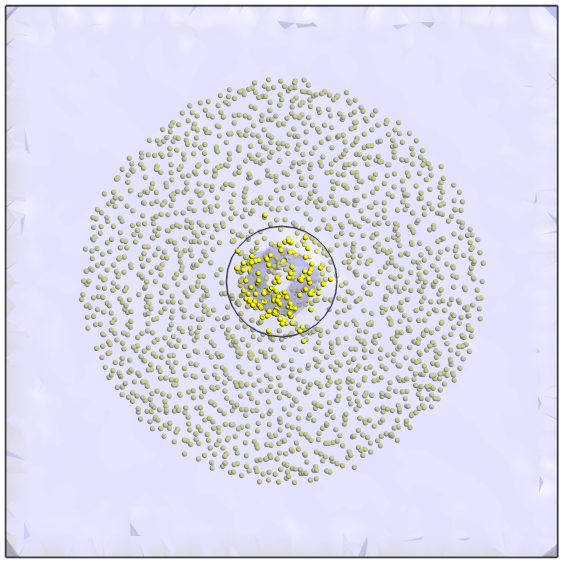

Figure 34: Top view $t^* = 55.4$

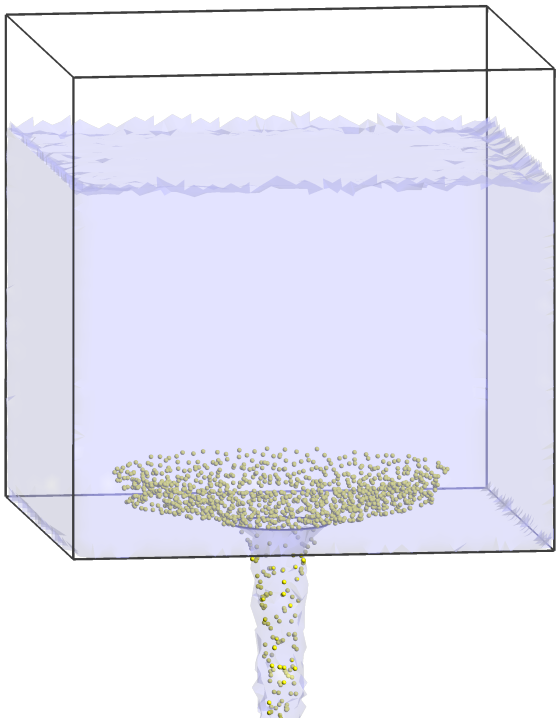

Figure 35: 3D view $t^* = 66.4$

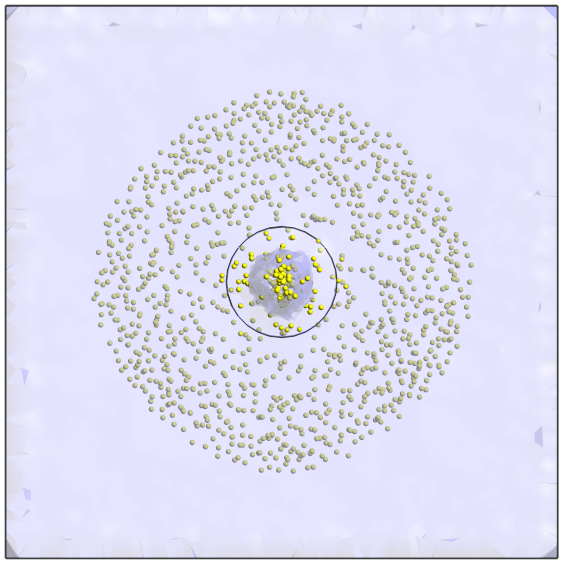

Figure 36: Top view $t^* = 66.4$

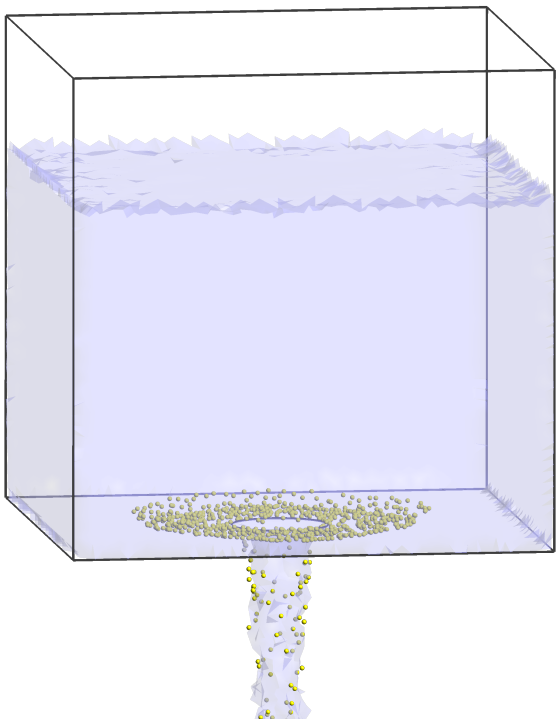

Figure 37: 3D view $t^* = 77.5$

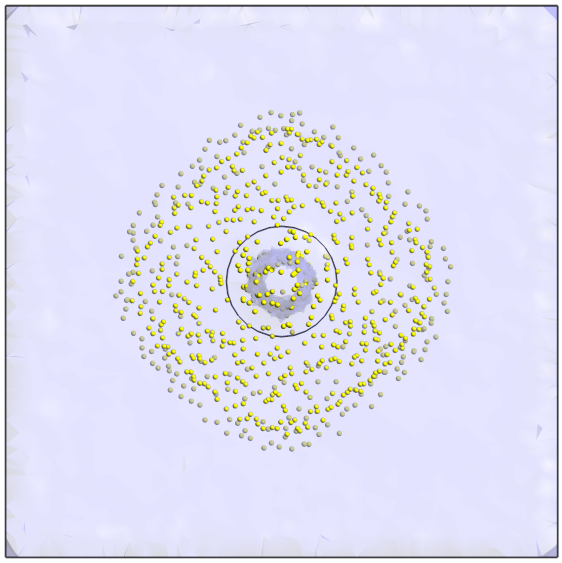

Figure 38: Top view $t^* = 77.5$

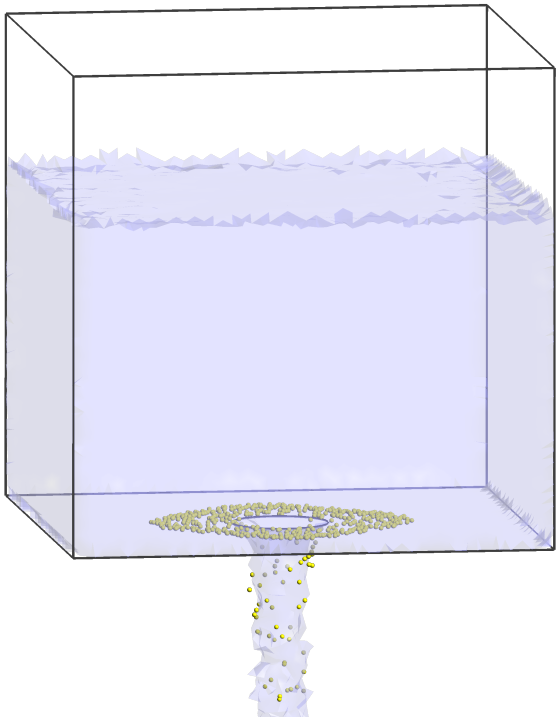

Figure 39: 3D view $t^* = 88.6$

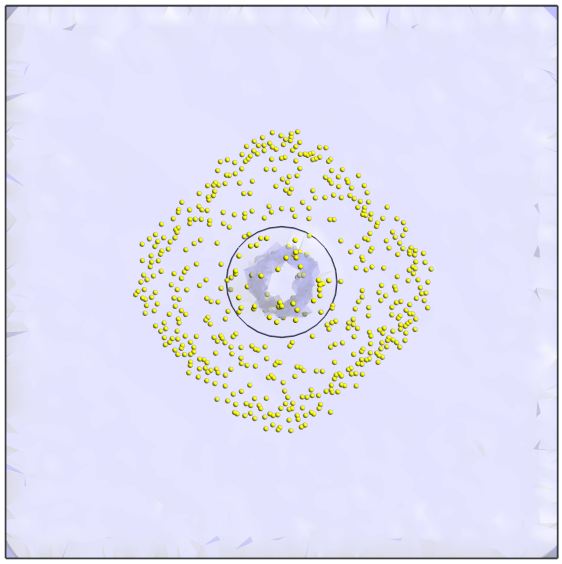

Figure 40: Top view $t^* = 88.6$

As it can be seen in the set of snapshots, the fluid experiments an acceleration because of the small cross section located at the bottom. For the fluid particles near to free surface,

the velocities are not so high, which explains why the initial cylinder made of solid particles does not suffer deformation in its shape at the beginning of the simulation.

When the DEM particles get closer to the orifice, as in the case of the fluid, they accelerate and cylinder is deformed. Those which are near to the center of the orifice, move faster than the ones located near to the lateral walls of the tank. Finally, the aforementioned particles far from the orifice, impact with the bottom part of the container, this is a logic behaviour because in this simulation the solid particles have a higher density of the fluid, so they reach more velocity than it. At the end, the particles which impact with the rigid surface are dragged to the hole. In the next set of figures 41-44, the results for a density $\rho^* = 1.5$ is presented:

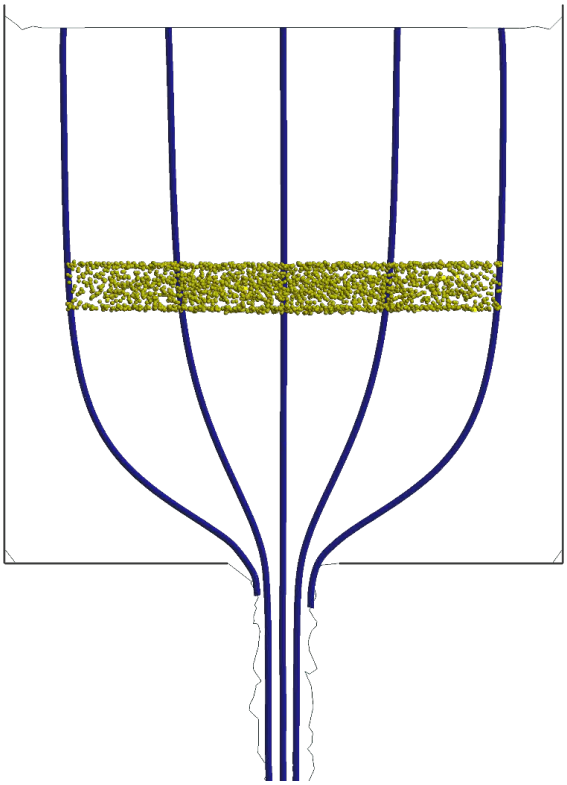

Figure 41: Lateral view $t^* = 11.1$

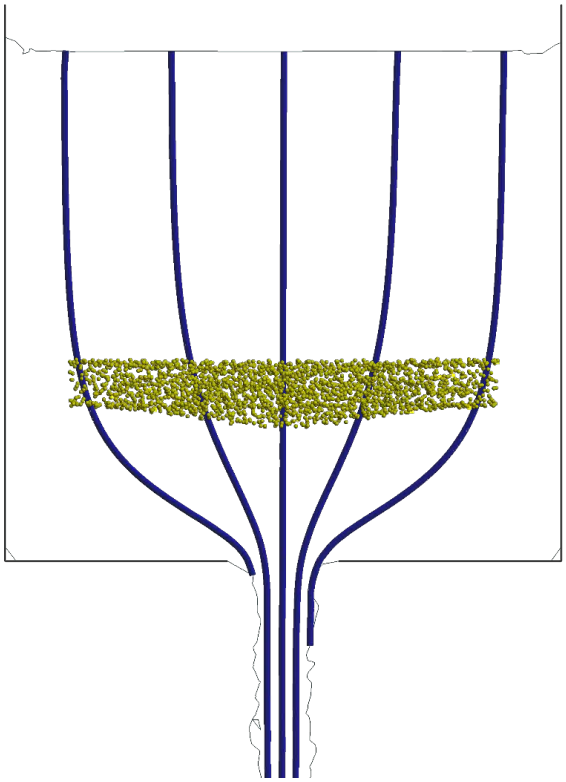

Figure 42: Lateral view $t^* = 22.1$

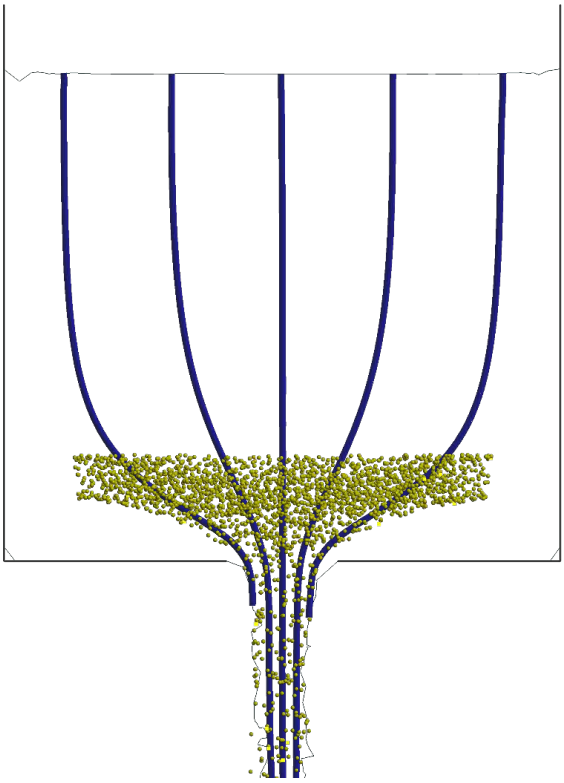

Figure 43: Lateral view $t^* = 33.2$

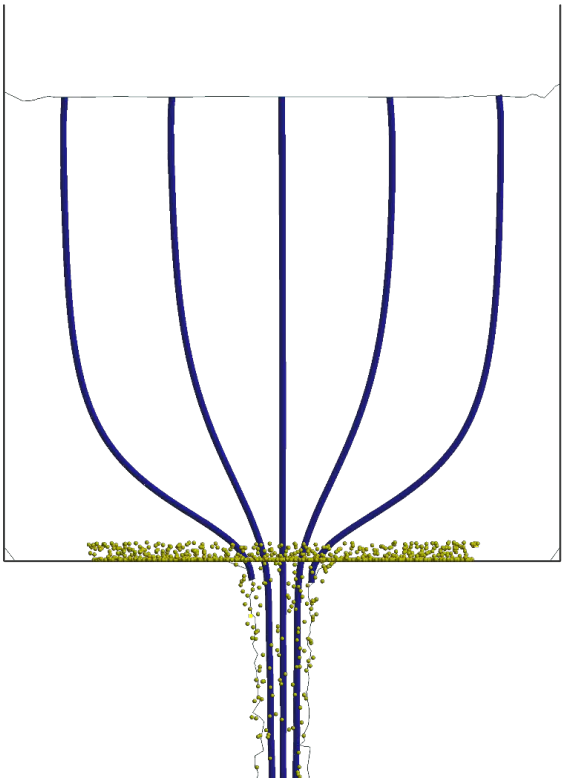

Figure 44: Lateral view $t^* = 44.3$

In this case, the particles move faster due to the increase of its density, in fact, less of them are dragged to the orifice and the time necessary to evacuate all them increases. Obviously, the higher is the density of the particles, the lower DEM particles follow the streamlines of the fluid. Finally, the results for DEM particles which have the same density as water are displayed in figures 45-48:

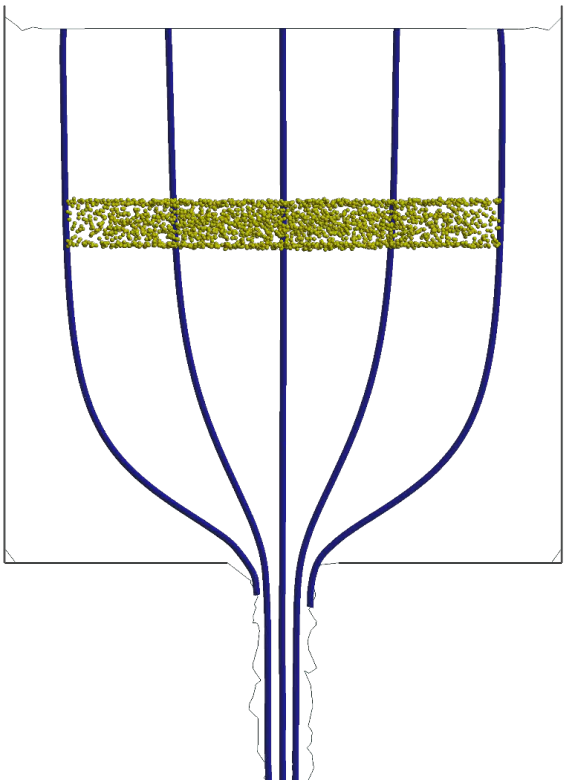

Figure 45: Lateral view $t^* = 11.1$

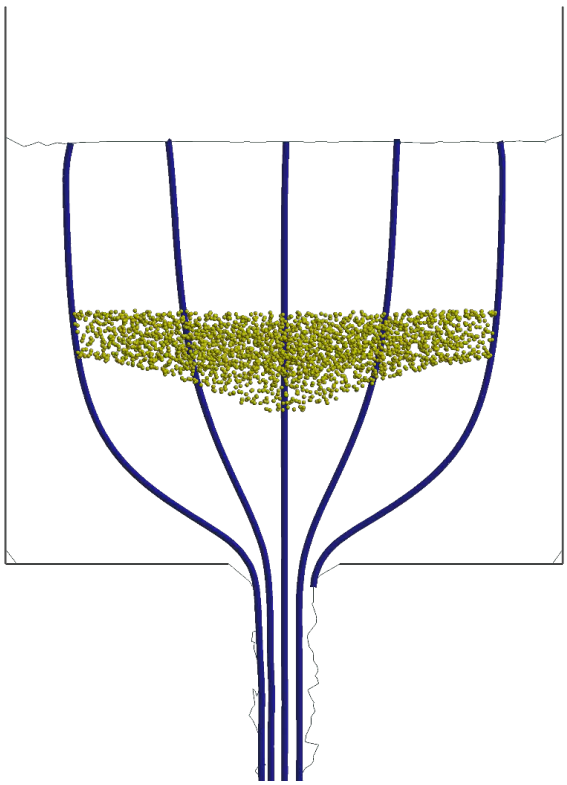

Figure 46: Lateral view $t^* = 66.4$

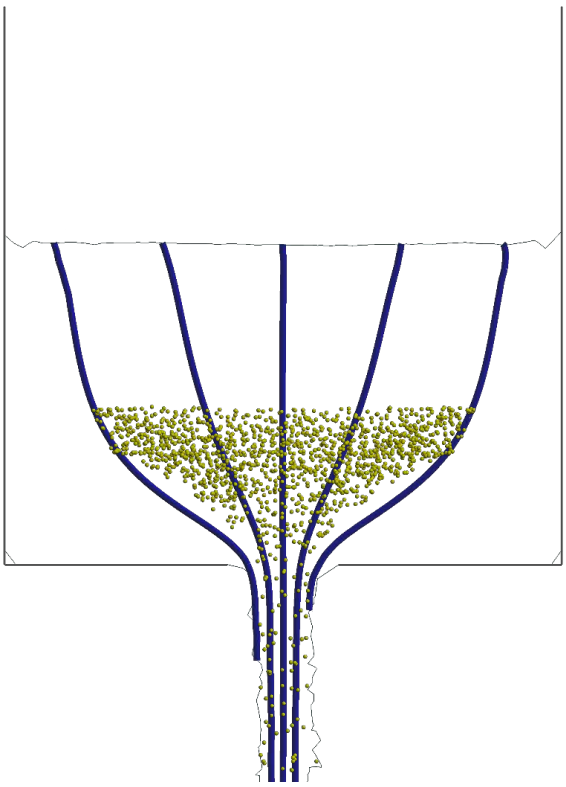

Figure 47: Lateral view $t^* = 121.8$

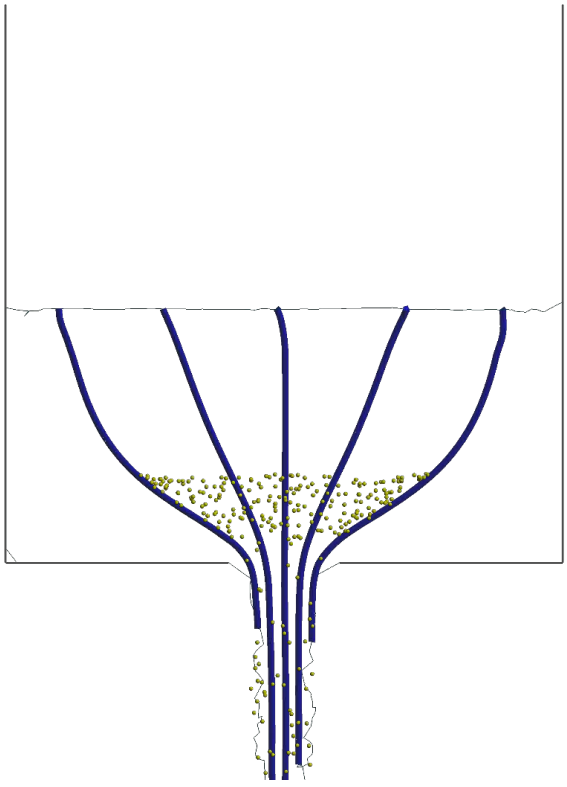

Figure 48: Lateral view $t^* = 166.1$

This results show the accuracy of the solution proposed. When the particles have the same density as fluid they follow perfectly the streamlines of it which results in a strong evidence that DEM can be applied as tracers of the fluid when PFEM is used. The PFEM nodes cannot be used for this purpose because the mesh of the fluid moves and remesh after the time step with the objective of guarantee a mesh quality. This last target is done by relocating the nodes from high nodes density areas to low density zones.

To verify the accuracy of the fluid solution, the Bernoulli's theorem will be used. Following this theorem, the outlet velocity of an inviscid and incompressible fluid contained in a tank has this expression

$$u = \sqrt{2gh_{fs} + u_{fs}^2} \tag{76}$$

in which h_{fs} is the height difference between the free surface level and the outlet velocity measurement. However, this relation is only valid if the difference of the pressure between the free surface and the place where velocity is evaluated can be neglected. To check it, in the following figures 49-52 the pressure field is plotted:

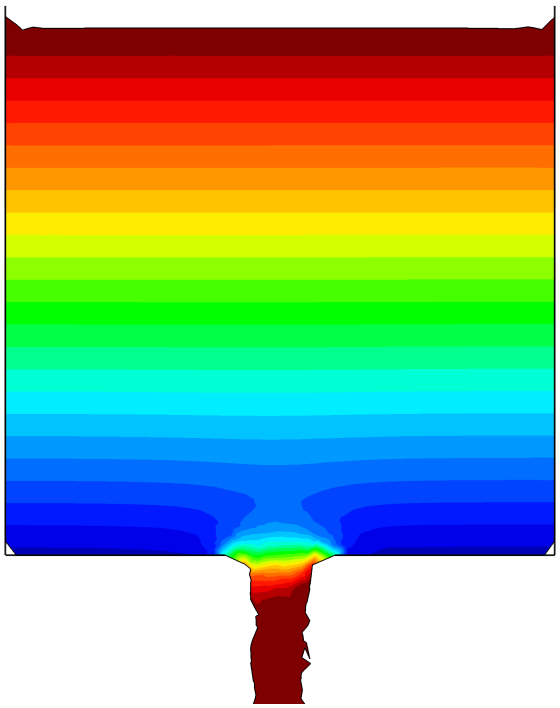

Figure 49: Lateral view $t^* = 11.1$

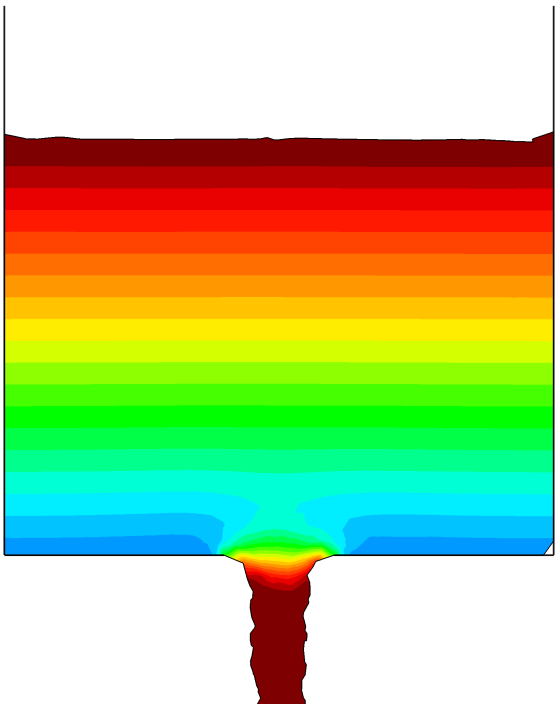

Figure 50: Lateral view $t^* = 66.4$

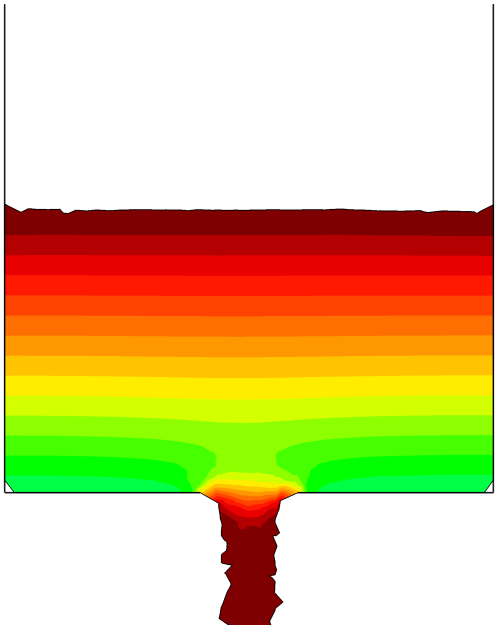

Figure 51: Lateral view $t^* = 121.8$

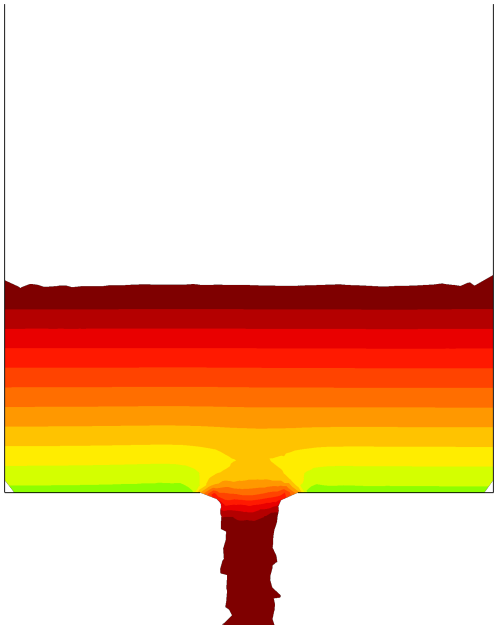

Figure 52: Lateral view $t^* = 166.1$

In the set of figures, the field pressure in a vertical cross section over the center of the orifice is evaluated. Far from the orifice, the pressure distribution is similar to a field produced in a hydrostatic case. Near to the hole, the discharge of water creates a perturbation of pressures with the same size as the orifice. When water leaves the container, water pressure is almost null, so the variation between the free surface and the zone below the tank is negligible. It can be concluded, that equation (75) can be used to evaluate the velocity in the water stream.

Figure 53 shows the dimensionless velocity of the DEM particle in the simulation when $\rho^* = 1.0$ in different points of water. For example, it can be noted that for the point $y^* = 1$, an important acceleration appears due to the approximation of the particle to the orifice after moving almost constantly from its initial position to the first point evaluated. When the velocity is measured at $y^* = -0.5$ another change of regime can be detected, the particle has left the tank so it starts to experiment a free fall with a constant acceleration similar to g.

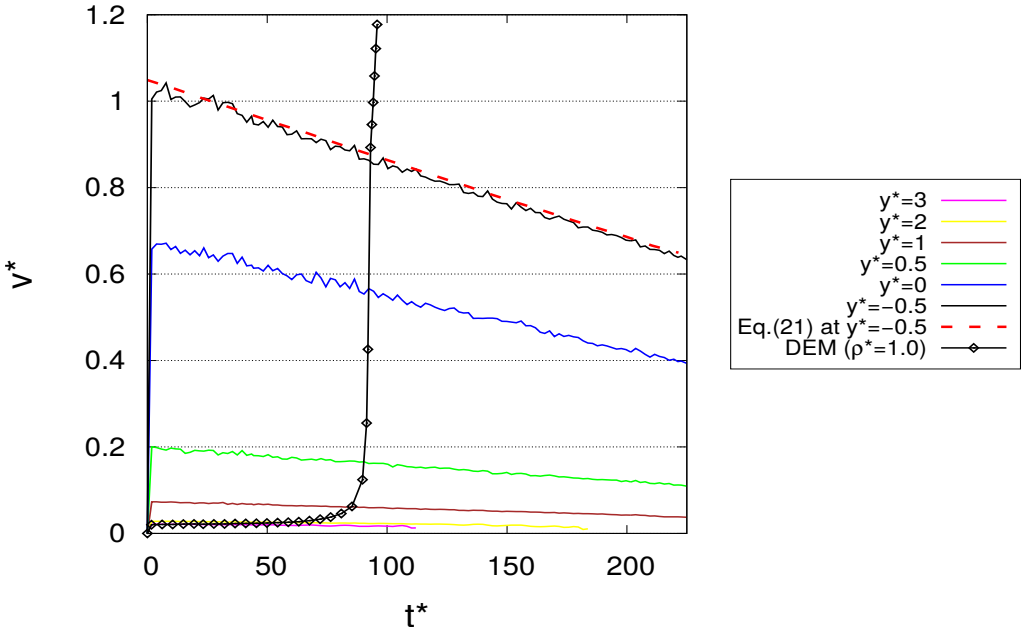

Figure 53: Evolution in time of the dimensionless velocity of water in different positions and a DEM particle of $\rho^* = 1.0$

Although the graphic only shows results of particle with a specific density, the same results are got for the analysis of the particles for $\rho^* = 1.125$ and $\rho^* = 1.50$. After having a constant velocity at the beginning of the simulation (higher velocity when density is higher), the acceleration starts to increase abruptly when the distance to the orifice is equal to the diameter of it before converging to g when the particles leaves the water tank. The evolution of the position and the velocity of a particles for three different density values is shown in figures 54 and 55 as follows:

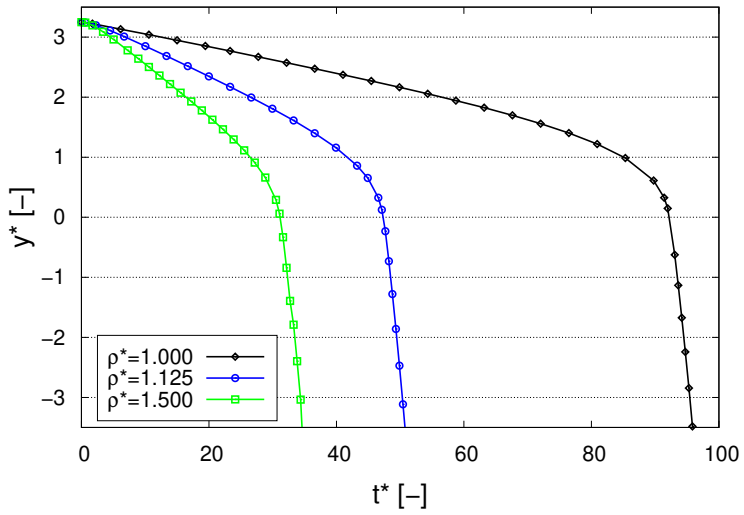

Figure 54: Evolution in dimensionless time of the dimensionless position for particles with different densities

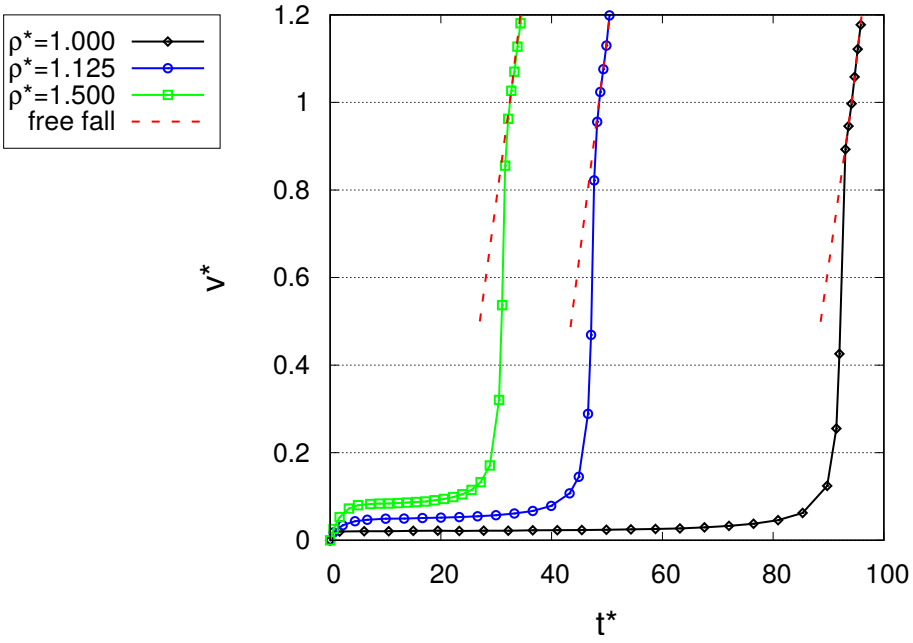

Figure 55: Evolution in dimensionless time of the dimensionless velocity for particles with different densities

To study the convergence of the PFEM DEM scheme four meshes have been analysed for the simulations using a particle density of $\rho^* = 1.0$ and $\rho^* = 1.5$. These meshes are compound by 1249676, 480698, 233411 and 109483 tetrahedra each one. Figures 56 and 57 shows the different phases of the particle settlement in which has been used the logarithmic scale for the vertical axis to make clearer the convergent behavior of the scheme used.

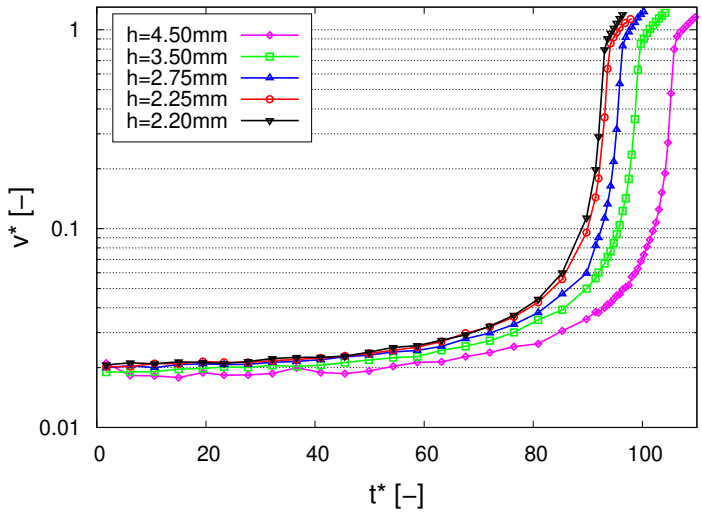

Figure 56: Dimensionless velocity of the sample using different meshes and a particle with $\rho^* = 1.0$

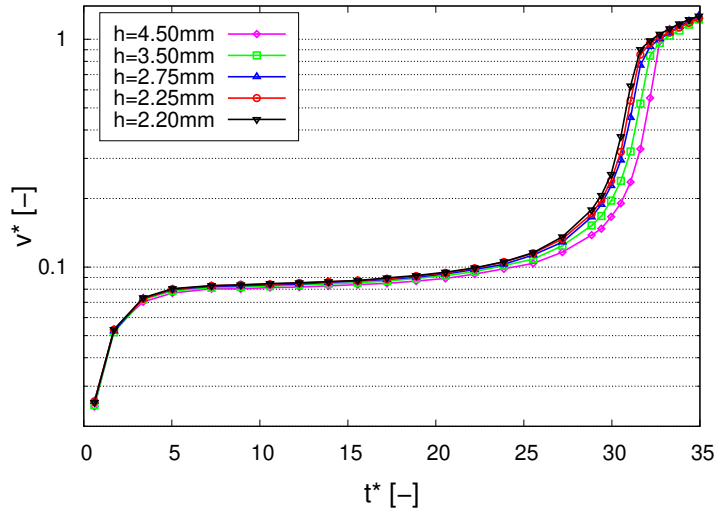

Figure 57: Dimensionless velocity of the sample using different meshes and a particle with $\rho^* = 1.5$

To finish the validation, the evolution on time of the fluid fluid mass leakage through the hole has been analyzed. The fluid mass remaining in the tank can be obtained using expression (71) together with the continuity equation. Therefore, the dimensionless water mass content can be computed as

$$M^*(t) = \frac{1}{H}\left(\sqrt{H} - \frac{A_o}{2}\sqrt{\frac{2g}{A_{fs}^2 - A_o^2}}t\right)^2 \tag{77}$$

where $A_{fs} = 1m^2$ is the area of the free surface and $A_o = C_d\pi D^2/4$ is the effective area of the hole. In the case of sharp orifices, C_d tends to be considered to have a value between 0.60 and 0.65. In the present document has been considered $C_d = 0.61$. In Figure 58, the dimensionless mass of the fluid in the tank is compared with the analytical solution provided by (76).

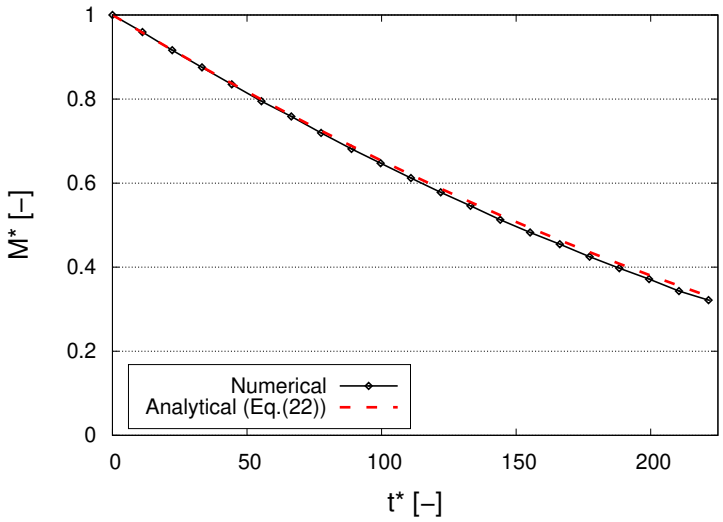

Figure 58: Time evolution of the dimensionless water mass in the tank

As it can be seen both, the numerical and analytical solution agree in the solution which proves the capability of PFEM to analyse the effective area of leakage in tank discharge problems.

5 Conclusions and Future lines

5.1 Conclusions

In this document, a fully Lagrangian fluid for numerical simulation to model the fluid surface has been carried out. The examples presented have consisted in problems in which the solid particles are small and disperse enough to disregard the effect of them in the fluid so one way coupling is suitable to provide accurate results.

To model the fluid, the PFEM has been computed using an implicit segregated solver based on two step, first the velocity is computed and them the pressure. To model the solid particles, DEM has been considered using a sub-stepping algorithm to obtain the convergence of them.

Regarding the presented examples, we have shown that the sedimentation of a sphere has been modelled successfully and verified with the Stoke's drag law which can be used for fluid with a low Reynolds number. In the second test, a dam break problem in 3D has been solved to show the capability of the scheme used to simulate an unsteady regime including an impact with a rigid wall. The solution has been validate with experimental results showing the good agreement with them. The solid particles have been implemented in order to compare the results obtained for them with future simulations.

The last test consisted in simulate a discharge of a water tank with a orifice at the bottom on it simulating the so-called *vena contracta*. A set of particles with different densities has been used. It has been checked that particles with same density as fluid can be used as a tracers of the streamlines to make it easier to analyse the fluid solution. The convergent behavior of the scheme used has been studied as well. Now, the ALE formulation and an example using ALE scheme as a future line which is being developed is shown.

5.2 ALE formulation

From two configurations that exist, the continuum domain is discretized. Apart from the aforementioned Lagrangian approach, in the Eulerian one the mesh is fixed and the fluid moves through it. Hence, the continuum is defined by its spatial coordinates regarding the mesh as the reference. In ALE, a third one can be considered in which the mesh can move with an arbitrarian velocity which is not equal to fluid. In conclusion, regarding w as the velocity of the mesh and v as the fluid velocity, three different cases can be found [4]:

a) $w = 0$, the reference configuration is fixed in the space, this case corresponds to the Eulerian configuration.

b) $w = v$, in this case the mesh moves at the same velocity as the fluid particles, thus it is the Lagrangian configuration.

c) $w \neq v \neq 0$, the mesh moves at an arbitrary velocity which is neither 0 nor the fluid one. In this case, the position of the variables are defined by the position vector ξ.

In the same way as the Jacobian determinant matches the infinitesimal volumes or areas (depending on it is a bidimensional or tridimensional problem) and the cartesian or natural coordinates [40], this determinant lets make a relation between the area or volume in mixed coordinates with its homologous in material coordinates, therefore

$$|J| = \frac{dV_o}{dV} \tag{78}$$

where dV is the infinitesimal volume in the mixed system and dV_o the one in material coordinates. To obtain the local form of governing equations, both are multiplied by the Jacobian determinant that, as it is above mentioned, relates the mixed variables with the material ones. Hereafter, the steps to obtain the governing equations in ALE formulation will be shown:

5.2.1 Mass conservation law

$$\frac{\partial}{\partial t}(\rho|J|) = |J|\frac{\partial}{\partial x_j}(\rho(w_j - v_i)) \tag{79}$$

If the following properties are taken into account

$$\frac{\partial}{\partial t}(|J|\rho) = |J|\left[\frac{\partial \rho}{\partial t} + \nabla \cdot (\rho w)\right] \tag{80}$$

$$|J|\nabla \cdot (\rho w) = \frac{\partial |J|}{\partial t}\rho + |J| w \cdot \nabla p \tag{81}$$

equation (80) can be written substituting expressions (81) and (82) in it as

$$\begin{aligned} |J|\nabla \cdot (\rho w) &= |J|\nabla \cdot (\rho w) - |J|\nabla \cdot (\rho v) \Rightarrow \\ |J|\left[\frac{\partial \rho}{\partial t} + \nabla \cdot (\rho w)\right] &= \frac{\partial |J|}{\partial t}\rho + |J| w \cdot \nabla p - |J| w \cdot \nabla p \end{aligned} \tag{82}$$

using the expression (83)

$$\nabla \cdot (\rho w) = \rho \nabla \cdot w + w \cdot \nabla \rho \tag{83}$$

substituting the property (83) in the first an the second term of the equation (82)

$$|J|\left[\frac{\partial \rho}{\partial t} + \rho \nabla \cdot w + w \cdot \nabla \rho\right] = \frac{\partial |J|}{\partial t}\rho + |J| w \cdot \nabla p - |J|\rho \nabla \cdot v - |J| v \cdot \nabla \rho \tag{84}$$

in addition, from [4] can be obtained

$$\frac{\partial |J|}{\partial t} = |J| \nabla \cdot w \tag{85}$$

substituting equation (85) in the Jacobian time derivative in the second term of the expression (84)

$$|J| \left[\frac{\partial \rho}{\partial t} + \rho \nabla \cdot w + w \cdot \nabla \rho \right] = |J| \nabla \cdot (w\rho) + |J| w \cdot \nabla p - |J| \rho \nabla \cdot v - |J| v \cdot \nabla \rho \tag{86}$$

if equation (83) is again substituted in the second term of the expression (86), the equation (87) is

$$|J| \left[\frac{\partial \rho}{\partial t} + \rho \nabla \cdot w + w \cdot \nabla \rho \right] = |J| [\rho \nabla \cdot w + w \cdot \nabla \rho + w \cdot \nabla \rho - \rho \nabla \cdot v - v \cdot \nabla \rho] \tag{87}$$

as it is shown in the equation (87), the Jacobian determinant can be removed in both sides of the equation. The second and the third summand of the left side and the first and second ones of the right side can be removed as well. Therefore

$$\frac{\partial \rho}{\partial t} = (w - v) \cdot \nabla \rho - \rho \nabla \cdot v \tag{88}$$

it can be detected from the last expression the mass conservation law, but now it is written in ALE formulation where, as it is explained before, w is the mesh velocity and v is the velocity of the fluid particle. As a consequence, in the Lagrangian approach, the convective term is not taken into account wich it makes this formulation simpler to model than the Eulerian one.

5.2.2 Momentum conervation law

Once the mass conservation law is obtained, the same will be done for the equation (75), hence, multiplying it by the Jacobian determinant

$$\begin{aligned} \frac{\partial}{\partial t} (\rho v_i |J|) &= |J| \frac{\partial}{\partial x_j} (\rho v_i (w_j - v_j)) + |J| (b_i - \frac{\partial p}{\partial x_i}) \Rightarrow \\ \rho |J| \frac{\partial v_i}{\partial t} + v_i \frac{\partial}{\partial t} (\rho |J|) &= |J| \rho (w - v) \frac{\partial}{\partial x_j} v_i + v_i |J| \frac{\partial}{\partial x_j} (\rho (w - v)) + |J| (b_i - \frac{\partial p}{\partial x_i}) \end{aligned} \tag{89}$$

substituting the second summand of expression (89) by equation (79), it is obtained

$$\rho |J| \frac{\partial v_i}{\partial t} + v_i |J| \frac{\partial}{\partial x_j} (\rho (w - v)) = |J| \frac{\partial}{\partial x_j} (\rho v_i (w - v)) + v_i |J| \frac{\partial}{\partial x_j} (\rho (w - v)) + |J| (b_i - \frac{\partial p}{\partial x_i}) \tag{90}$$

removing the second summand of the first term with the second one of the second term and the Jacobian

$$\rho\frac{\partial v_i}{\partial t} = \frac{\partial}{\partial x_j}\left(\rho v_i(w-v)\right) + (b_i - \frac{\partial p}{\partial x_i}) \tag{91}$$

finally, it is provided the momentum conservation law in ALE formulation

$$\rho\frac{\partial v_i}{\partial t} = \rho(w-v)\cdot\nabla v_i + (b_i - \frac{\partial p}{\partial x_i}) \tag{92}$$

The same conclusions are obtained as in the mass conservation law since the first summand of equation (92) is removed when the Lagrangian configuration is used simplifying the equation.

In this work, the element used to compute the ALE approach is the QSVMS based on the variational multiscale method (VMS) which can be found in [41].

5.3 Example to validate

The example used to perform the coupling is a rotating drum which consists in a small cylinder whose rigid walls rotate with a constant angular velocity. The objective of this example is to compare the results with the ones performed in [42] and the experiment carried out in [43]. In this example, the rotator drum is a cylinder of $D = 0.1m$ whose generatrix length is the same as the diameter. The geometry of the example can be seen in Figure 59. This case has been used to test ALE strategy because the rotation in the rigid walls affects mainly in the free surface while in the rest of the fluid domain the remesh is not necessary.

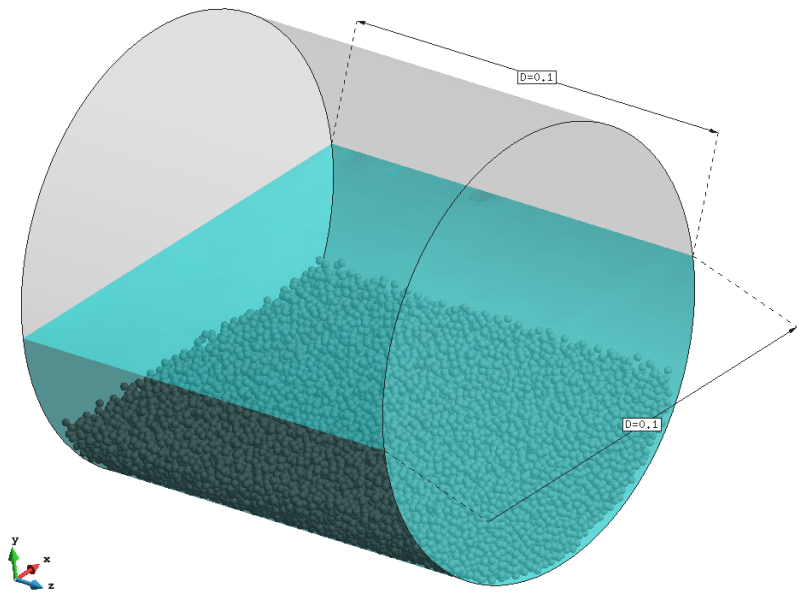

Figure 59: Initial position of the rotator drum

The fluid simulates water with density of $\rho_f = 1000kg/m^3$ and a viscosity of $\mu = 8.9 \cdot 10^{-4}Pa \cdot s$. The number of particles are 30891 to guarantee a total mass of 200 grams as it is set in [42]. In this case the drag law used is Beetstra drag law which can be found in [44]. This law is used for cases in which there are a huge accumulation of particles.

With the purpose of obtaining a good convergence in the fluid solution, angular velocity is increasing gradually from $w = 2rad/s$ to the maximum velocity $w = 10.89rad/s$. When $t = 0.198s$ after this time step, the angular velocity is kept constant. To set the Lagrangian and Eulerian approach in the fluid, the first layer of nodes of the continuum has been considered as free surface (Lagrangian approach) whereas the rest of them (including the nodes which interact with the rigid walls) have been regarded as non free surface (Eulerian scheme). In Figure 60, this criteria can be seen:

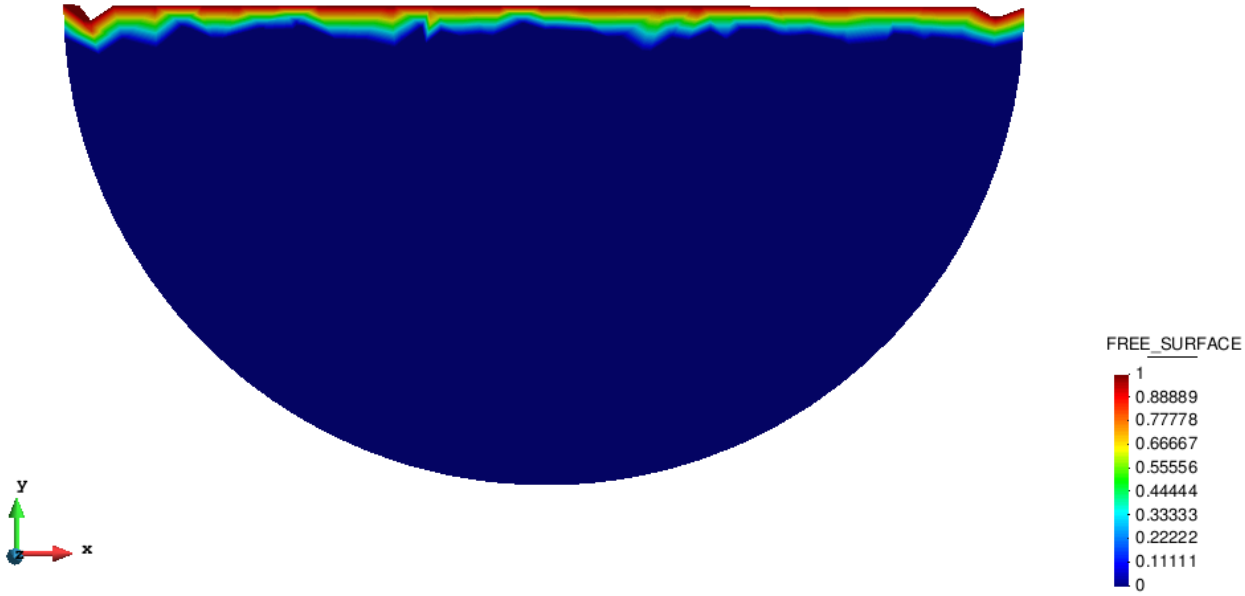

Figure 60: Limit between the Lagrangian (in red) and Eulerian (in blue) schemes

As it can be seen in figures 61 and 62, the results obtained from the simulation and those provided by experiment are different, showing the limitations of one-way coupling for the cases in which the amount of particles are relevant to interact with the fluid. The results are compared qualitatively.

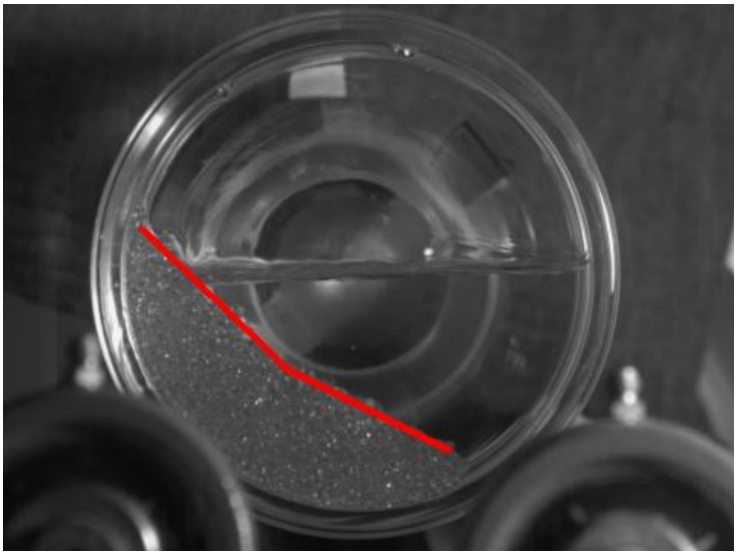

Figure 61: Experimental results [43]

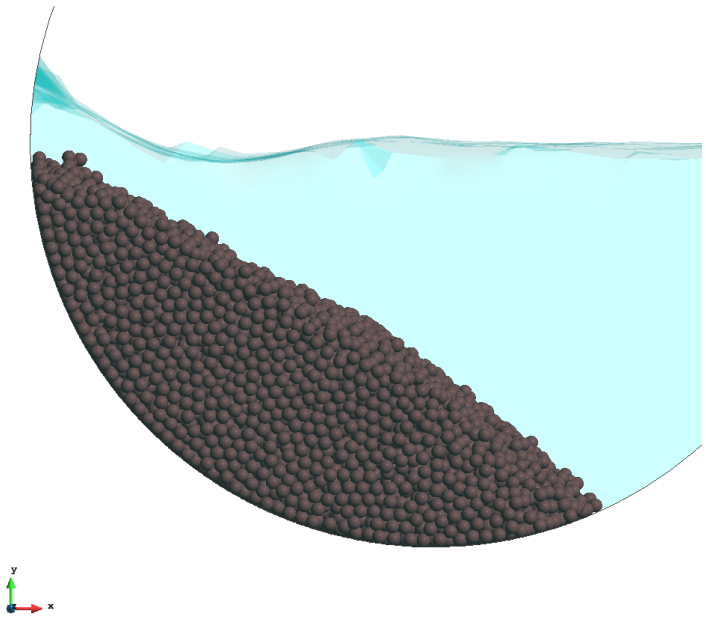

Figure 62: Solution obtained from numerical simulation (one-way)

Finally, other research lines consist in getting a two-way strong PFEM-DEM coupling for both, two step v-p and ALE formulation. The objective is to be able to simulate those cases in which the effect of the particles cannot be negligible as in the rotating drum or a dam break with a bed of particles at the bottom. In this line, not only the transfer of forces from DEM particles to fluid is being developing but the porosity of the solid phase which will let PFEM fluid to simulate a flow through a porous media. An application of it in which we are working is the placement of dredging material when it is discharged from a pipeline located on the top of water, information of this process called convective descend can be found in [45]. In the model, a closed area simulating a dock is plenty of water with a orifice

in one of the faces of the container to evacuate the fluid, an inlet of particles denser than water are falling from the top on the opposite side of the hole. The purpose is to fill the dock of solid particles substituting water by them. This process is used in harbors to drain docks. The final objective is to analyse the influence of water flow in the angle of the cone produced by the settlement of particles and the zones where this inlet could be located in order to optimize the time needed to remove water. In Figure 63 is shown a snapshot with preliminary results of a current simulation that is being carried out.

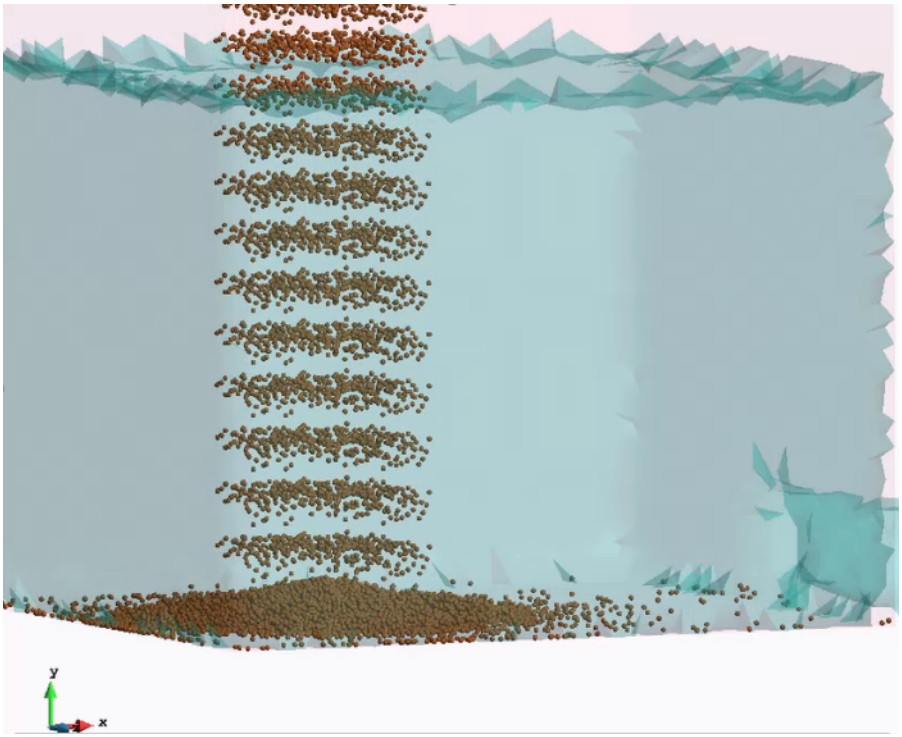

Figure 63: Result obtained from simulation (two-way)

5.4 Contributions

The main contributions of the author in this work can be summarized in the present list:

1. One way coupling between PFEM and DEM. Coupling the two applications to make the transfer of information from the application that computes the fluid to the solid particle for both scheme, ALE and free-surface fluid.

2. Designing examples to do the simulation and compare the results with the ones in literature (as in the case of rotator drum).

3. Developing two way coupling weak between PFEM and DEM. In this case, the work is in progress and it is needed to perform more simulations to validate the coupling. Two way coupling implies a transfer from DEM to PFEM after the solution of solid

particles including the porosity, so the fluid flow can be affected by the presence of DEM particles.

4. Designing examples to simulate draining of docks

5. Correcting bugs found in the applications.

References

[1] T Belytcshko and J M Kennedy. Finite element study of pressure wave attenuation by reactor fuel subassemblies. *Journal of pressure vessel technology*, (97):172–177, 1975.

[2] W F Noh. A time-dependent two-space dimensional, coupled Eulerian-Lagrangian code. *Methods in computational Physics (Acedemic Press New York)*, page 117, 1964.

[3] C W Hirt, A A Amsdem, and J L Cook. An Arbitrarian Lagrangian-Eulerian computing method for all flow speeds. *Journal of computational physics*, (14):227–253, 1974.

[4] J Donea, S Giuliani, and J P Halleux. An arbitrary Lagrangian-Eulerian finite element method for transient dynamic fluid-structure interactions. *Computer method in applied mechanics and engineering*, (33):689–723, 1982.

[5] H H Hu, D D Joseph, and M J Crochet. Direct simulation in fluid particle motions. *Theoretical and computational fluid dynamics*, (3):285–306, 1992.

[6] Q Zhang and T Hisada. Analysis of fluid-structure interaction problems with structural buckling and large domain changes by ALE finite element method. *Computational methods in applied mechanics and engineering*, (190):6341–6357, 2001.

[7] F Del Pin, S Idelsohn, E Oñate, and R Aubry. The ALE/Lagrangian Particle Finite Element Method: A new approach to computation of free-surface flows and fluid-object interactions. *Computers & fluids*, (36):27–38, 2007.

[8] S R Idelsohn, E Oñate, and F Del Pin. The particle finite element method: a powerful tool to solve incompressible flows with free-surfaces and breaking waves. *International journal for numerical methods in engineering*, (61):964–989, 2004.

[9] R A Gingold and J J Monaghan. Smoothed particle hydrodynamics: theory and application to non-spherical stars. *Monthly Notices of the Royal Astronomical Society*, (181):375–389, 1977.

[10] B Nayroles, G Touzot, and Villon P. Generalizing the finite element method: Diffuse approximation and diffuse elements. *Computational Mechanics*, (10):307–318, 1992.

[11] E Oñate, S Idelsohn, O C Zienkiewicz, and R L Taylor. A finite point method in computational mechanics. Applications to convective transport and fluid flow. *International journal for numerical method in engineering*, 39:3839–3866, 1996.

[12] E Oñate, S R Idelsohn, and M A Celigueta. Modeling bed erosion in free surface flows by the particle finite element method. *Acta Geotechnica*, (1):237–252, 2006.

[13] E Oñate, S R Idelsohn, M A Celigueta, and R Rossi. Advances in the particle finite element method for the analysis of fluid-multibody interaction and bed erosion in free surface flows. *Computer methods in applied mechanics and engineering*, (197):1777–1800, 2008.

[14] E Oñate, M A Celigueta, S R Idelsohn, F Salazar, and B Suárez. Possibilities of the particle finite element method for fluid-soil-structure interaction problems. *Computationan Mechanics*, (48):307–318, 2011.

[15] P A Cundall and O D L Strack. A discrete numerical model for granular assemblies. *Géotechnique*, 29(1):47–65, 1979.

[16] E Oñate and J Rojek. Combination of discrete element and finite element methods for dynamic analysis of geomechanics problems. *Computer methods in applied mechanics and engineering*, (193):3087–3128, 2004.

[17] A A Johnson and T E Tezduyar. Simulation of multiple spheres falling in a liquid-filled tube. *Computer methods in applied mechanics and engineering*, (134):351–373, 1996.

[18] T I Zohdi. Computation of strongly coupled multifield interaction in particle-fluid systems. *Computer methods in applied mechanics and engineering*, (196):3927–3950, 2007.

[19] B Avci and P Wriggers. A DEM-FEM coupling approach for the direct numerical simulation of 3D particulate flows. *Journal of applied mechanics*, (79):7, 2012.

[20] M A Celigueta, K M Deshpande, S Latorre, and E Oñate. A FEM-DEM technique for studying the motion of particles in non-Newtonian fluids. application of the transport of drill cuttings in wellbores. *Computational particle mechanics*, (3):263–276, 2016.

[21] S R Idelsohn, J Marti, A Limache, and E Oñate. Unified Lagrangian formulation for elastic solids and incompressible fluids: Application to fluid-structure interaction problems via PFEM. *Computer methods in applied mechanics and engineering*, (197):1762–1776, 2008.

[22] E Oñate, J García, S R Idelsohn, and F Del Pin. Finite calculus formulations for finite element analysis of incompressible flows. Eulerian, ALE and Lagrangian approaches. *Computer methods in applied mechanics and engineering*, (195):3001–3037, 2006.

[23] E Oñate, A Franci, and J M Carbonell. Lagrangian formulation for finite element analysis of quasi-incompressible fluid with reduced mass losses. *Internation journal for numerical methods in fluids*, (74):699–731, 2014.

[24] E Oñate. Derivation of stabilized equations for numerical solution of advective-diffusive transport and fluid flow problems. *Computer methods in applied mechanics and engineering*, (151):233–265, 1998.

[25] I de Pouplana and E Oñate. A FIC-based stabilized mixed finite element method with equal order interpolation for solid-pore fluid interaction problems. *International journal for numerical and analytical methods in geomechanics*, 41(1), 2017.

[26] H Edelsbrunner and T Seng Tang. An upper bound for conforming Delaunay triangulations. *Discrete & computational geometry*, (10):197–213, 1993.

[27] H Edelsbrunner and E P Mucke. Three-Dimensional Alpha Shape. *ACM Trans Graphics*, (13):43–72, 1994.

[28] E Loth and A J Dorgan. An equation of motion for particles of finite Reynolds number and size. *Environmental Fluid Mechanics*, (9):187–206, 2009.

[29] L Wakaba and S Balachandar. On the added mass force at finite reynolds and acceleration numbers. *Theoretical and Computational fluid dynamics*, (21.2):147–153, 2007.

[30] L Schiller and A Naumann. A drag coefficient correlation. *Zeitschrift des Vereins Deutscher Ingenieure*, (7):318–320, 1935.

[31] G Casas, D Mukherjee, M A Celigueta, T I Zohdi, and E Oñate. A modular, partitioned, discrete element framework for industrial grain distribution systems with rotating machinery. *Computational particle mechanics*, (4):181–198, 2017.

[32] E Hairer, C Lubich, and G Wanner. Geometric numerical integration illustrated by the Störmer–Verlet method. *Acta Numerica*, (12):399–450, 2003.

[33] R J Williams, E Perkins, and B Cook. A contact algorithm for partitioning N arbitrary sized objects. *Engineering Computations*, (21):235–248, 2004.

[34] S Koshizuka and Y Oka. Moving-particle semi-implicit method for fragmentation of incompressible fluid. *Philosophical Nuclear science and engineering*, (123):421–434, 1996.

[35] Alessandro Franci, Ignasi de Pouplana, Guillermo Casas, Miguel Ángel Celigueta, Joaquín González-Usúa, and Eugenio Oñate. PFEM–DEM for particle-laden flows with free surface. *Computational Particle Mechanics*, 2019 (Submitted in May 2019).

[36] M Robinson, M Ramaioli, and S Luding. Fluid-particle flow simulations using two-way-coupled mesoscale SPH-DEM and validation. *International Journal of Multiphase Flow*, (59):121–134, 2014.

[37] J C Martin and W J Moyce. An experimental study of the collapse of liquid columns on a rigid horizontal plane 4. *Philosophical Transactions of the Royal Society of London*, (Series A, 244):312–324, 1952.

[38] S Koshizuka and Y Oka. Moving-particle semi-implicit method: fully Lagrangian analysis of incompressible flows. *Proceedings of the European Congress on Computational Methods in Applied Sciences adn Engineering (ECCOMAS), Barcelona (Spain)*, 2000.

[39] C Hu and M Sueyoshi. Numerical simulation and experiment on dam break problem. *Journal of Marine Science and Application*, (9):109–114, 2010.

[40] E Oñate. *Structural analysis with the Finite Element Method. Linear Static*, volume 1. Springer, first edition, 2009.

[41] J Cotela. Applications of Turbulence Modeling in Civil Engineering. *Doctoral Thesis. Barcelona: Universitat Politècnica de Catalunya*, 2016.

[42] Y He, A E Bayly, A Hassanpour, Muller F, K Wu, and Yang D. A GPU-based coupled SPH-DEM method for particle-fluid flow with free surfaces. *Powder Technology*, (338):548–562, 2018.

[43] X Sun, M Sakai, and Y Yamada. Three-dimensional simulation of a solid-liquid flow by the DEM-SPH method. *Journal of Computational Physics*, (248):147–176, 2013.

[44] Renske Beetstra. *Drag force in random arrays of mono- and bidisperse spheres*. PhD thesis, University of Twente, Netherlands, 2005.

[45] *EM 1110-2-5025 Dredging and Dredged Material Management Engineering Manual*, (Chapter 3), 2015.